Journal of Advanced Research xxx (xxxx) xxx

Contents lists available at ScienceDirect

Journal of Advanced Research

journal homepage: www.elsevier.com/locate/jare

Design of a targeted dual drug delivery system for boosting the efficacy of photoimmunotherapy against melanoma proliferation and metastasis

Yi Chen [a,1], Shan Xu [a,1], Shuang Ren [a,f,1], Jiyuan Zhang [e], Jinzhuan Xu [a], Yuxuan Song [a,f], Jianqing Peng [a], Shuai Zhang [d,*], Qianming Du [b,c,*], Yan Chen [a,f,*]

[a] State Key Laboratory of Functions and Applications of Medicinal Plants, School of Pharmaceutical Sciences, Guizhou Medical University, Guiyang 561113, China
[b] General Clinical Research Center, Nanjing First Hospital, Nanjing Medical University, Nanjing 210006, China
[c] School of Basic Medicine & Clinical Pharmacy, China Pharmaceutical University, Nanjing 210009, China
[d] Department of Interventional Radiology, The Affiliated Hospital of Guizhou Medical University, Guiyang 550004, China
[e] School of Pharmacy, Fudan University, Shanghai 201203, China
[f] Key Laboratory of Novel Anti-Cancer Drug Targets Discovery and Application, School of Pharmaceutical Sciences, Guizhou Medical University, Guizhou 561113, China

HIGHLIGHTS

- Combination of purpurin 18 and epacadostat in photoimmunotherapy for melanoma.
- The pH sensitivity of borate ester to implement an enhanced-targeting strategy.
- Hyaluronic acid modification to achieve long circulation and enhanced EPR effects.
- Enhanced internalization of tumor cells by precise targeting of salivary acid residues.
- Induced anti-tumor immunity to inhibit melanoma proliferation and metastasis.

GRAPHICAL ABSTRACT

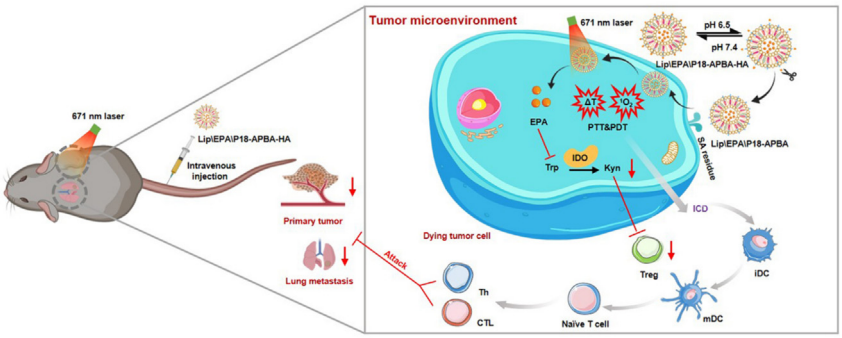

ARTICLE INFO

Article history:
Received 1 April 2024
Revised 16 May 2024
Accepted 17 May 2024
Available online xxxx

Keywords:
Photoimmunotherapy
Melanoma
pH-triggered delivery
Indoleamine-2
3 dioxygenase inhibitor
Purpurin 18

ABSTRACT

Introduction: The combination of a photosensitizer and indoleamine-2,3 dioxygenase (IDO) inhibitor provides a promising photoimmunotherapy (PIT) strategy for melanoma treatment. A dual drug delivery system offers a potential approach for optimizing the inhibitory effects of PIT on melanoma proliferation and metastasis.

Objective: To develop a dual drug delivery system based on PIT and to study its efficacy in inhibiting melanoma proliferation and metastasis.

Methods: We constructed a multifunctional nano-porphyrin material (P18-APBA-HA) using the photosensitizer-purpurin 18 (P18), hyaluronic acid (HA), and 4-(aminomethyl) phenylboronic acid (APBA). The resulting P18-APBA-HA was inserted into a phospholipid membrane and the IDO inhibitor epacadostat (EPA) was loaded into the internal phase to prepare a dual drug delivery system (Lip\EPA \P18-APBA-HA). Moreover, we also investigated its physicochemical properties, targeting, anti-tumor immunity, and anti-tumor proliferation and metastasis effects.

Results: The designed system utilized the pH sensitivity of borate ester to realize an enhanced-targeting strategy to facilitate the drug distribution in tumor lesions and efficient receptor-mediated cellular

* Corresponding authors at: General Clinical Research Center, Nanjing First Hospital, Nanjing Medical University, Nanjing 210006, China (Q. Du). Department of Interventional Radiology, the Affiliated Hospital of Guizhou Medical University, Guiyang 550004, China (S. Zhang). State Key Laboratory of Functions and Applications of Medicinal Plants, School of Pharmaceutical Sciences, Guizhou Medical University, Guiyang 561113, China (Y. Chen).
E-mail addresses: zhangshuai476900@gmc.edu.cn (S. Zhang), duqianming@njmu.edu.cn (Q. Du), s0710189@sina.com (Y. Chen).
[1] Y. Chen, S. Xu, and S. Ren contributed equally to this work.

https://doi.org/10.1016/j.jare.2024.05.017

endocytosis. The intracellular release of EPA from Lip\EPA\P18-APBA-HA was triggered by thermal radiation, thereby inhibiting IDO activity in the tumor microenvironment, and promoting activation of the immune response. Intravenous administration of Lip\EPA\P18-APBA-HA effectively induced anti-tumor immunity by promoting dendritic cell maturation, cytotoxic T cell activation, and regulatory T cell suppression, and regulating cytokine secretion, to inhibit the proliferation of melanoma and lung metastasis. *Conclusion:* The proposed nano-drug delivery system holds promise as offers a promising strategy to enhance the inhibitory effects of the combination of EPA and P18 on melanoma proliferation and metastasis.

Introduction

Melanoma is a malignant skin cancer that originates from normal melanocytes or primitive nevi in the epidermis [1,2]. This type of cancer is characterized by a high metastatic capability and a low cure rate, necessitating the development of effective therapies targeting its rapid growth and high metastasis. Melanoma is a highly immunogenic tumor, and the advent of immunotherapy has provided new opportunities for its treatment; however, the complex nature of the immunosuppressive tumor microenvironment (ITM), as well as problems with off-target drug delivery, have resulted in low immunotherapy response and cure rates for melanoma [3,4].

Photoimmunotherapy (PIT) is an anti-tumor therapy that combines phototherapy with immunotherapy. It has demonstrated the ability to enhance the immune stimulation response by eliminating solid tumors and restricting tumor metastasis [5,6]. Phototherapy encompasses photothermal therapy (PTT) and photodynamic therapy (PDT), and simultaneous triggering of PDT and PTT can effectively compensate for the lack of efficacy associated with tumor hypoxia and the short life span of $^1O_2$ during standalone PDT treatment. Meanwhile, the addition of PDT can also reduce the heat shock protein-mediated thermotolerance of tumor cells to PTT [7–9]. Additionally, phototherapy has been shown to not only eliminate tumor cells, but also induce an immune response to tumor-associated antigens (TAAs), which rupture cancer cells and generate danger-associated molecular patterns (DAMPs). This immunogenic cell death (ICD) induced by phototherapy contributes to the inhibition of distant tumor metastasis [10,11]. Purpurin 18 (P18), a dihydroporphyrin derivative of chlorophyll, exhibits strong singlet to triplet transitions and non-radiative decay, enabling simultaneous realization of both PDT and PTT. Compared with single PDT or PTT, P18-mediated dual-modal phototherapy induces a more potent immune response, potentially leading to inhibition of cancer metastasis [12–14]. However, the immune response induced by phototherapy is weak and insufficient to eliminate the risk of melanoma proliferation and metastasis, due to the ability of tumor cells to utilize various immune escape mechanisms in the tumor microenvironment (TME), such as up-regulating the expression of relevant proteins to alter the metabolic behaviors of tumor cells or immune cells, thus allowing tumor cells to evade immune system recognition and severely limiting anti-tumor efficacy [15,16].

Modulating the immune response by altering the metabolism of immune cells is an attractive strategy [17]. Indoleamine-2,3 dioxygenase (IDO) is an essential enzyme in immune cell metabolism that catalyzes the conversion of tryptophan (Trp) to kynurenine (Kyn). Trp deficiency accelerates the growth of regulatory T cells (Tregs) but inhibits the activation of cytotoxic T cells (CTLs), and IDO is thus considered to be a major culprit of the ITM [18,19]. Clinical studies showed that IDO inhibitors such as epacadostat (EPA), 1-methyl tryptophan, and NLG919 effectively inhibited IDO activity, blocked the IDO pathway, and inhibited tumor cell immune evasion, thereby enhancing the efficacy of anti-tumor therapy [20]. However, EPA failed in phase III clinical trials, mainly because of the limited capacity for IDO inhibition at the tumor site. Enhancing drug penetration and cell internalization at tumor sites using targeting nanocarriers is thus considered to be an effective strategy to restore the inhibitory potential of IDO inhibitors at tumor sites [21,22].

An ideal targeted nanomaterial delivery system must consider the accumulation and retention of materials in tumor tissues mainly dependent on enhanced permeability and retention (EPR) effects, as well as cellular internalization of targeted ligand modifications [23,24]. However, traditional surface modification strategies make it difficult to achieve both these effects simultaneously. Enhanced-targeting is a recent novel, two-stage targeting strategy based on a stimulus–response system. The nanocarrier system design utilizes stimulation-responsive nanomaterials and includes activated surface ligands and other properties [25,26]. For instance, hyaluronic acid (HA) is a hydrophilic linear disaccharide polymer that improves tumor targeting and biocompatibility of nanoparticles and extends their circulation time in the body. HA can specifically target the CD44 receptor on the surface of TME tumor cells. However, HA is prone to rapid degradation in tumor sites, limiting the ability of the nanoformulations to target cell internalization [27,28]. On the other hand, some small molecular targets, such as sialic acid (SA) residues, are overexpressed on the cell membrane due to abnormal glycosylation and are specifically recognized in melanoma cells. Although SA residues can be targeted by antibodies, lectins, or phenylboronic acid (PBA). However, normal tissues also express SA residues to a certain extent, leading to off-target effects [29–31]. Nanocarriers with high stability in the blood circulation and structural transformation under stimulation by the TME (exposing small molecular ligands) may thus effectively improve the tumor accumulation, retention, and penetration, as well as other capabilities of the nanocarriers. This enhanced-targeting strategy is achieved in two stages: (1) prolonging the circulation time *in vivo* by modification of the hydrophilic materials (such as HA), and then targeting tumor tissues based on the EPR effect, and (2) targeting tumor cells using small molecule targeting ligands (such as PBA).

We initially utilized P18, HA, and 4-(aminomethyl) PBA (APBA) to construct a multifunctional nanoporphyrin material (P18-APBA-HA). The P18-APBA-HA was then inserted onto the surface of liposomes and loaded with the IDO inhibitor EPA, to construct an HA-modified nano-delivery system (Lip\EPA\P18-APBA-HA) (Scheme 1). We propose that the combination of a photosensitizer and an IDO inhibitor provides a promising PIT strategy for melanoma treatment and that a dual drug delivery system offers a potential approach to optimizing the inhibitory effects of PIT on melanoma proliferation and metastasis. It is worth noting that this study is the first to report the rational design of such a system and provide relevant *in vitro* and *in vivo* data to support its potential applications.

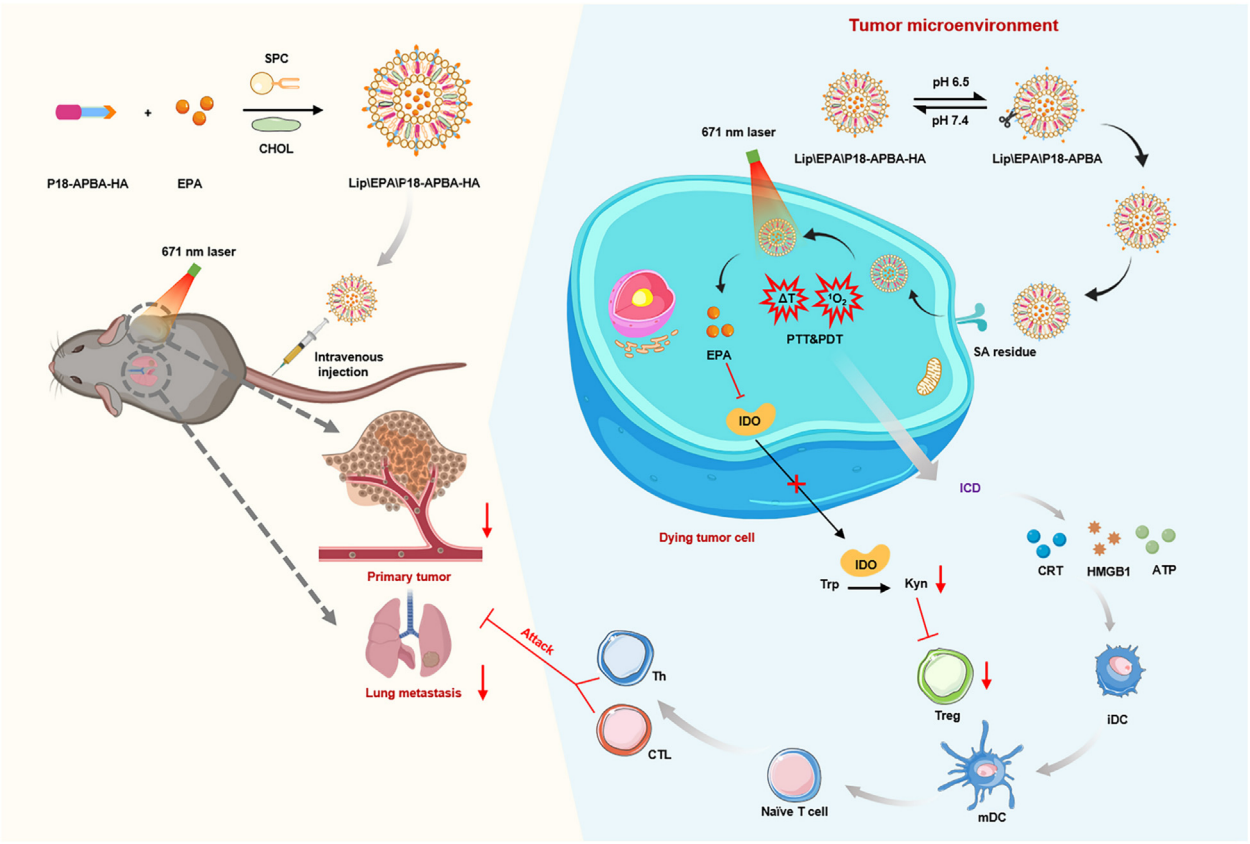

Scheme 1. Schematic illustration of Lip\EPA\P18-APBA-HA preparation and its mechanism for inhibiting primary tumors and lung metastasis based on PIT. After intravenous administration, Lip\EPA\P18-APBA-HA aggregated at the tumor region, aided by its long circulation and EPR effect. The weakly acidic TME and the SA residues on the tumor cell surface will cause cleavage of the *iso*-PBA ester bond of P18-APBA-HA, and the HA will be stripped off, thereby exposing the PBA group. The PBA group could then be specifically recognized by the SA residues on the surface of the melanoma cells, thus enhancing their specific uptake of the nanoparticles. Following laser irradiation, the heat and ROS generated by P18 resulted in tumor cell death and the release of large amounts of TAAs and EPA. The released TAAs activated the immune response and stimulated the formation of effector T cells, while the EPA released in the TME increased the viability of effector T cells by inhibiting IDO activity and the immune evasion of tumor cells.

Materials and methods

Chemicals and reagents

EPA and P18 were obtained from Zhengzhou Alfa Chemical Co., Ltd. (Zhengzhou, China). APBA was purchased from Shanghai Haohong Biomedical Technology Co., Ltd. (Shanghai, China). HA was obtained from Bloomage Freda Biopharma Co., Ltd. (Jinan, China). 4-Dimethylaminopyridine (DMAP) was provided by Adamas-beta (Shanghai) Chemical Reagent Co., Ltd. (Shanghai, China). 1-Ethyl-3-(3-dimethyllaminopropyl) carbodiimide hydrochloride (EDCI) and Rhodamine B (RB) were provided by Macklin Biochemical Co., Ltd. (Shanghai, China). Cholesterol (CHOL) was purchased from Sigma-Aldrich (St. Louis, MO, USA). Soybean phospholipids (SPC) were purchased from A.V.T. (Shanghai) Pharmaceutical Co., Ltd. (Shanghai, China). Cyanine 5.5 (Cy5.5) was provided by Xi'an RuiXi Biological Technology Co., Ltd. (Shaanxi, China). Immunostaining fixative, Hoechst 33342, reactive oxygen species (ROS) assay kit, Cell Counting Kit-8 (CCK-8), and red blood cell lysate were obtained from Beyotime Biotechnology Inc. (Shanghai, China). The chemiluminescent adenosine triphosphate (ATP) assay kit, high-mobility group box 1 (HMGB1), Trp, Kyn, tumor necrosis factor-alpha (TNF-α), interleukin 6 (IL-6), and interferon-gamma (IFN-γ) enzyme-linked immunosorbent assay (ELISA) kits were supplied by ZCIBIO Technology Co., Ltd. (Shanghai, China). 2′,7′-Dichlorofluorescin diacetate (DCFH-DA) was obtained from Shanghai Aladdin Biochemical Technology Co., Ltd. (Shanghai, China). Calreticulin (CRT) polyclonal antibody (Cat. No. 27298–1-AP), anti-CD11c-fluorescein isothiocyanate (FITC) (Cat. No. 65130), anti-CD40-phycoerythrin (PE) (Cat. No. PE-65062), anti-CD80-PE (Cat. No. PE-65076), anti-CD86-allophycocyanin (APC) (Cat. No. APC-65068), anti-CD3-APC (Cat. No. APC-65060), anti-CD4-FITC (Cat. No. PE-65104), anti-CD8a-PE (Cat. No. PE-65069), and anti-Foxp3-PE (Cat. No. PE-65089) antibodies were all from Proteintech Group, Inc. (Wuhan, China). Alexa Fluor 488-goat anti-rabbit IgG (Cat. No. AB150077) was supplied by Abcam plc. (Cambridge, UK). Hematoxylin and eosin (H&E) stains were provided by KeyGEN Biotech Inc. (Nanjing, China). Aspartate aminotransferase (AST) and alanine aminotransferase (ALT) test kits were obtained from Derui Biotechnology, Co., Ltd. (Shenzhen, China).

Cells and animals

The mouse melanoma cell line B16F10 cells and the mouse dendritic cell (DC) line DC2.4 cells were purchased from the American Tissue Culture Collection (Rockville, MD, USA) and Shanghai Jinyuan Biotechnology Co., Ltd. (Shanghai, China), respectively. The cells were cultured in the medium (RPMI 1640, Gibco, Invitrogen Corporation, NY, USA) supplemented with 10 % (v/v) fetal bovine serum (FBS, Cellmax, Lanzhou, China) and 1 % streptomycin/penicillin and were maintained in 5 % CO_2 at 37 °C.

C57BL/6 mice (6–8 weeks old, 18–22 g, female; Certificate No. SCXK2021-0013) were obtained from Changzhou Cavens Lab Animal Co., Ltd. (Jiangsu, China). All animal experiments were conducted strictly in accordance with the protocol approved by the

Animal Welfare and Ethics Committee of Guizhou Medical University (No. 1900118).

Synthesis of P18-APBA-HA conjugates

P18 (50 mg), EDCI (18.3 mg), and DMAP (11.5 mg) were dissolved in 2 mL of dimethylsulfoxide (DMSO), activated for 1 h, and APBA (56.4 mg) was then added. The mixture was stirred for 24 h at 25°C, dialyzed (MWCO 3.5 kDa) with water for 24 h, and freeze-dried to prepare amaranthine solid P18-APBA.

HA (40 mg) was dissolved in 2 mL formamide and P18-APBA (14 mg) was dissolved in 2 mL DMSO. The P18-APBA solution was then added dropwise to the HA solution with continuous stirring, followed by the addition of CaH_2, and adjustment to pH 9, and the solution was stirred at 65°C for 24 h. The mixture was dialyzed (MWCO 3.5 kDa) against water overnight and then freeze-dried to obtain olive green solid P18-APBA-HA. The resulting products were characterized by ^{1}H-nuclear magnetic resonance spectroscopy (AVANCE NEO 600 MHz, Bruker Corporation, Zurich, Switzerland).

Preparation of Lip\EPA\P18-APBA-HA

SPC (18 mg) and CHOL (2 mg) were dissolved in 2 mL of chloroform at a mass ratio of 9 : 1. The solvent was removed and dried in a rotary evaporator to form a film, and 4 mL of 250 mM $(NH_4)_2SO_4$ solution (containing 5 mg of P18-APBA-HA) was then added and hydrated at 40°C for 1 h. Lip\P18-APBA-HA was obtained after ultrasound treatment (300 W) ice-water bath (3 s pulse, 3 s pause) for 5 min using an ultrasonic cell disruptor (650E, Beidi Institute of Scientific Instruments Co., Ltd., Shanghai, China) and dialyzed (MWCO 14 kDa) with pH 7.4 phosphate-buffered saline (PBS) for 2 h. EPA solution (3 mg EPA dissolved in 20 μL DMSO) was then added dropwise to Lip\P18-APBA-HA with stirring, followed by 30 min incubation in a 40°C water bath. The DMSO and unencapsulated EPA were dialyzed (MWCO 3.5 kDa) against pH 7.4 PBS for 2 h to obtain Lip\EPA\P18-APBA-HA.

Characterization of liposomes

The diameter, polydispersity index (PDI), and zeta potential of the liposomes were determined using a dynamic laser scatterometer (90Plus PALS, Brookhaven Instruments Co., Ltd., NY, USA). Morphology images of Lip\EPA\P18, Lip\EPA\P18-APBA, and Lip\EPA\P18-APBA-HA were obtained by transmission electron microscopy (TEM, HT7800, Hitachi, Ltd., Tokyo, Japan).

The drug concentration of EPA in the liposomes was determined by high-performance liquid chromatography (HPLC, LC-16, Shimadzu Instruments Co., Ltd., Kyoto, Japan) using an ODS-3 C18 column (5 μm, 250 × 4.6 mm) with a mobile phase of 70% acetonitrile and 30% water at 290 nm. To detect P18, the optical density (OD) was measured by UV spectrophotometry (UV-2700, Shimadzu Instruments Co., Ltd.) at 406 nm. The loading capacity (LC) and loading efficiency (LE) of EPA and P18 were determined by the following equations:

$$\mathrm{LC}\ (\%) = \frac{W_{drug\ loaded}}{W_{total\ liposome}} \times 100 \quad (1)$$

$$\mathrm{LE}\ (\%) = \frac{W_{drug\ loaded}}{W_{drug\ added}} \times 100 \quad (2)$$

Photothermal performance in vitro

The photothermal performance was evaluated by detecting the temperature changes of various concentrations of P18 solutions when exposed to a laser (671 nm, 0.8 W/cm^2) for 5 min. The optimal concentration of P18 was then selected and irradiated with a 671 nm laser with different powers for 5 min to determine the optimal power for the photothermal conversion of P18. PBS was used as a control. The *in vitro* photothermal performances of EPA + P18, Lip\EPA\P18, Lip\EPA\P18-APBA, and Lip\EPA\P18-APBA-HA were examined in the same way. We also evaluated the photothermal stability of Lip\EPA\P18-APBA-HA by irradiation under the same conditions for 5 min at the optimal concentration and power, and turned off the laser for 5 min for cooling. The process was repeated four times, and the temperature was recorded every 30 s using an infrared thermal imaging system (PTi120, Fluke Corporation, WA, USA). ΔT was calculated as follows: $\Delta T = T_s - T_0$, where T_s and T_0 represent the temperature of the samples and the initial temperature, respectively).

pH-triggered diameter and zeta potential changes

Lip\EPA\P18-APBA-HA was added to PBS pH 6.5 or pH 7.4, respectively, and maintained at 37°C. The diameter and zeta potential of the liposomes were then measured at a predetermined time.

Drug release behavior

The drug release of EPA from Lip\EPA\P18-APBA-HA was evaluated by dialysis using PBS containing Tween 80 (0.25%, w/v) pH 5.5, 6.5, and 7.4, respectively, as the release medium. Liposomes irradiated with a 671 nm laser for 5 min at 0.8 W/cm^2 before dialysis were denoted as L+. The liposomes were loaded into dialysis bags (MWCO 3.5 kDa) and placed in 20 mL of release medium in a shaking incubator (100 rpm, 37°C). The medium was collected at the predetermined times and supplemented with an equal volume of fresh medium. Finally, the concentrations of EPA were determined using HPLC.

Cellular uptake

B16F10 cells (6 × 10^3 cells/well) were cultured in ViewPlate-96 microplates overnight, and treated with free RB, Lip\RB\P18, Lip\RB\P18-APBA, or Lip\RB\P18-APBA-HA (10 μg/mL RB and 0.5 μg/mL P18) for 2 or 4 h at pH 6.5, respectively. For the competitive assay, the cells were pre-incubated with HA or APBA for 30 min, followed by incubated with Lip\RB\P18-APBA-HA at pH 6.5 for 2 or 4 h. The cells were then rinsed with PBS and fixed with a 100 μL immunostaining fixative for 10 min, and stained with Hoechst 33,342 for 30 min. Finally, cellular uptake of liposomes was captured by a high-content imaging system (Operetta CLS, PerkinElmer Inc., Berlin, Germany) and estimated using ImageJ 1.8.0.

Intracellular ROS levels

B16F10 cells (6 × 10^3 cells/well) were cultured in ViewPlate-96 microplates overnight, and treated with PBS, EPA + P18, Lip\EPA\P18, Lip\EPA\P18-APBA, or Lip\EPA\P18-APBA-HA (2.5 μg/mL EPA and 0.5 μg/mL P18) at pH 6.5 for 4 h, respectively. After incubation, the cells were rinsed and incubated with 10 μM DCFH-DA at 37°C for 30 min in the absence of light. Some groups were also irradiated with a 671 nm laser irradiation (0.8 W/cm^2, 2 min). The cells were then cleaned, fixed, and stained, and intracellular ROS production was observed using a high-content imaging system and quantified using ImageJ 1.8.0.

Cytotoxicity assay

B16F10 cells were cultured in 96-well plates at a density of 5 × 10^3 cells per well overnight, and treated with P18,

EPA + P18, Lip\EPA\P18, Lip\EPA\P18-APBA, or Lip\EPA\P18-APBA-HA at pH 6.5 for 4 h. The cells were then subjected to 671 nm laser irradiation (0.8 W/cm^2, 2 min) or dark treatment for 24 h. After incubation, the medium was replaced with 100 μL medium (containing 10 μL CCK-8), and incubated for another 2 h. The OD value was recorded using a microplate reader at 450 nm (Infinite M200 Pro, Tecan Trading Co., Ltd., Männedorf, Switzerland), and the cell viability (%) was calculated according to the following equation:

$$\text{Cell viability } (\%) = \frac{\text{ODsample} - \text{ODcontrol}}{\text{ODnormal} - \text{ODcontrol}} \times 100 \quad (3)$$

ICD induction in vitro

CRT exposure was investigated using a high-content imaging system. Briefly, B16F10 cells were cultured in ViewPlate-96 microplates at a density of 1×10^4 cells per well overnight, and treated with PBS, P18, EPA + P18, Lip\EPA\P18, Lip\EPA\P18-APBA, or Lip\EPA\P18-APBA-HA (2.5 μg/mL EPA and 0.5 μg/mL P18) at pH 6.5 for 4 h. The medium was then replaced with fresh medium and A portion of the cells was then irradiated with a 671 nm laser (0.8 W/cm^2, 2 min). After 24 h, the cells were fixed and stained with CRT polyclonal antibody as well as Alexa Fluor 488-goat anti-rabbit IgG. Finally, the cells were stained with Hoechst 33,342 prior to observation using a high-content imaging system.

Extracellular levels of HMGB1 and ATP were measured using HMGB1 ELISA kits and chemiluminescent ATP assay kits, respectively. Briefly, B16F10 cells were inoculated in a 6-well plate and treated with PBS, EPA + P18, Lip\EPA\P18, Lip\EPA\P18-APBA, or Lip\EPA\P18-APBA-HA (2.5 μg/mL EPA and 0.5 μg/mL P18) at pH 6.5 for 4 h, washed, and added to fresh medium. A portion of the cells was then irradiated with a 671 nm laser (0.8 W/cm^2, 2 min). The supernatant was collected after 24 h, and HMGB1 and ATP were measured according to the manufacturer's protocols.

DC maturation and Try/Kyn ratio detection in vitro

To investigate the effect of Lip\EPA\P18-APBA-HA-treated B16F10 cells on DC maturation, the cells were initially treated with PBS, EPA + P18, Lip\EPA\P18, Lip\EPA\P18-APBA, or Lip\EPA\P18-APBA-HA (2.5 μg/mL EPA and 0.5 μg/mL P18) at pH 6.5 for 4 h followed by washing. Some cells were then irradiated with a 671 nm laser (0.8 W/cm^2, 2 min). After incubation for 24 h, the remaining cells were collected and co-cultured with DC2.4 cells for 24 h. The DC2.4 cells were then harvested and stained with anti-mouse CD80-PE and anti-mouse CD86-APC for 30 min. DC maturation was detected by flow cytometry (FCM) and determined using NovoExpress software (NovoCyte, ACEA Biosciences Inc., CA, USA). To measure the IDO inhibition effect, Trp and Kyn levels were determined in supernatants of treated DC2.4 cells using mouse Trp and Kyn ELISA kits, following the manufacturer's instructions.

Establishment of the B16F10 tumor-bearing mouse model

We established a B16F10 tumor-bearing mouse model by subcutaneous injection of female C57BL/6 mice with 5×10^5 B16F10 cells in the right front armpit. The mice were maintained until the tumor volume reached an appropriate for the experiment.

Biodistribution of Cy5.5-loaded liposomes

B16F10 tumor-bearing mice were separated into four groups randomly (n = 3) and injected intravenously with free Cy5.5, Lip\Cy5.5\P18, Lip\Cy5.5\P18-APBA, or Lip\Cy5.5\P18-APBA-HA solution (2 mg/kg Cy5.5 and 0.6 mg/kg P18), respectively. The mice were then anesthetized by isoflurane inhalation at a predetermined time, and fluorescent images were obtained and analyzed using an animal imaging system (ABL X1, Tanon, Shanghai, China). 24 h after injection, the mice were sacrificed, and the tumors and organs were collected, recorded, and imaged for *ex vivo* imaging.

Photothermal performance

B16F10 tumor-bearing mice were injected intravenously with PBS, EPA + P18, Lip\EPA\P18, Lip\EPA\P18-APBA, or Lip\EPA\P18-APBA-HA (3 mg/kg EPA and 0.6 mg/kg P18), respectively. After 12 h, the tumor site was irradiated for 2 min with a 671 nm laser (0.8 W/cm^2). The mice were then imaged and the temperature of the tumor region was recorded.

ROS detection

DCFH-DA acts as a probe to detect ROS production *in vivo*. B16F10 tumor-bearing mice were injected intravenously with PBS, EPA + P18, Lip\EPA\P18, Lip\EPA\P18-APBA, or Lip\EPA\P18-APBA-HA (3 mg/kg EPA and 0.6 mg/kg P18), respectively. After 12 h, DCFH-DA was injected intratumorally, followed by laser irradiation (671 nm, 0.8 W/cm^2, 2 min) of the tumor site. Finally, the mice were sacrificed, and the tumors were isolated and rinsed, followed by frozen sections and Hoechst 33,342 staining, and examined with confocal laser scanning microscopy (CLSM, LSM800, Carl Zeiss Meditec AG, Jena, Germany).

Efficacy against primary tumors

B16F10 tumor-bearing mice were separated into 7 groups (n = 6) randomly and injected intravenously with PBS, EPA + P18, Lip\EPA\P18, Lip\EPA\P18-APBA, or Lip\EPA\P18-APBA-HA (3 mg/kg EPA and 0.6 mg/kg P18), respectively. After 12 h, the tumor site was irradiated with a 671 nm laser (0.8 W/cm^2) for 2 min. The drug was administered every 2 days, and the body weight and tumor volume were measured every other day during treatment. All the mice were killed on day 14, and the tumors, tissues, tumor-draining lymph nodes (TDLNs), and blood samples were harvested for subsequent evaluation.

IDO inhibitory effect

After treatment, mouse tumor tissues were removed, homogenized, and the supernatant was separated by centrifugation at $3000 \times g$ for 10 min. Trp and Kyn were detected using ELISA kits.

Anti-tumor immune response

The TDLNs were ground and centrifuged to obtain cell suspensions. DCs were stained with anti-CD11c-FITC, anti-CD40-PE, anti-CD80-PE, and anti-CD86-APC antibodies and detected by FCM. The collected tumor tissues were also used to analyze the intratumoral infiltration of T lymphocytes and analyzed by FCM. Briefly, tumor tissues were ground, lysed, and centrifuged to obtain cell suspensions. The tumor lymphocytes were stained by using anti-CD3-PAC and anti-CD4-FITC antibodies to analyze T helper (Th) cells ($CD3^+$ $CD4^+$), anti-CD3-APC and anti-CD8a-PE antibodies to analyze CTLs ($CD3^+$ $CD8^+$), and anti-CD4-FITC and anti-Foxp3-PE antibodies to analyze Tregs ($CD4^+$ $Foxp3^+$). The serum levels of IL-6, TNF-α, and IFN-γ were determined by ELISA kits.

Anti-metastasis efficacy

To investigate the potential anti-metastasis efficacy, we injected each mouse (5×10^5 cells/mouse) with B16F10 cells intravenously when the primary tumor volume reached 90 mm^3. The

mice were then separated into seven groups (n = 6) randomly and treated with the same dosage regimens as for the anti-primary tumor. All the mice were killed on day 14, the lungs were removed, sectioned, and stained with H&E.

Lungs from each group were ground and centrifuged to form cell suspensions. DCs were stained with anti-CD11c-FITC, anti-CD40-PE, anti-CD80-PE, and anti-CD86-APC antibodies, and analyzed by FCM. The infiltration of CTLs ($CD3^+$ $CD8^+$) in the lung was also analyzed using anti-CD3-APC and anti-CD8a-PE antibodies.

Statistical analysis

The results were expressed as the mean ± standard deviation (SD). Results were compared between groups by one-way ANOVA followed by *post hoc* Tukey–Kramer test. The difference was considered significant when $p < 0.05$.

Results and discussion

Synthesis of P18-APBA-HA

The synthesis scheme of P18-APBA-HA conjugated with a pH-responsive PBA ester bond is illustrated in **Fig. S1**. Briefly, the synthesis process consisted of two steps: first, P18-APBA synthesis was catalyzed by EDCI and DMAP and then linked with HA to form P18-APBA-HA. The structures of P18-APBA and P18-APBA-HA were confirmed by ^{1}H-nuclear magnetic resonance spectroscopy (**Fig. S2**). The peaks observed at 6.5–8.0 and 9.25 ppm belonged to functional APBA fragments while other proton signals belonged to P18 fragments. The amide proton signal peak at 9.25 ppm demonstrated the linkage of APBA and P18. P18-APBA was able to form a covalent bond with the HA diol group. The characteristic HA peaks were evident at 1.82 ppm (methylproton of N-acetyl group, $-NHCOCH_3$) and 3.30–4.58 ppm (hydroxyl and methylene groups of polysaccharide backbone). Furthermore, the methyl proton peak of P18 was observed at 1.02–1.30 ppm, and the characteristic phenyl peak at 7.92–8.31 ppm.

Preparation and characterization of Lip|EPA|P18-APBA-HA

In this study, P18-APBA-HA with a PBA ester bond was synthesized and utilized as a modified material for liposomes to construct an HA-modified multi-level targeted nano-delivery system Lip\EPA\P18-APBA-HA. The diameter of Lip\EPA\P18-APBA-HA was slightly larger (approximately 180 nm) compared with blank or unmodified liposomes. The diameter distribution of the liposomes was within the range of 143–180 nm, consistent with the passive targeting particle size range of 100–200 nm. The PDI of all liposomes was lower than 0.3, indicating that the formulation process was stable and the liposomes had a smaller particle size distribution (Fig. 1**A**). All drug-loaded liposomes exhibited a negative charge, with Lip\EPA\P18-APBA-HA having the lowest surface zeta potential, possibly due to the surface modification of P18-APBA-HA (Fig. 1**B**). Although EPA exhibited a certain degree of hydrophobicity, its dispersion and encapsulation efficiency through the film were low. Furthermore, Badiee et al. found that EPA could be effectively encapsulated via the ammonium sulfate gradient method [32]. EPA passed through the phospholipid bilayer of the liposome, became ionized in the acidic environment of the inner aqueous phase, and salted with sulfate, which prevented EPA from passing through the phospholipid bilayer again and was loaded in the inner aqueous phase of the liposome. P18-APBA-HA was shown to improve hydrophilicity because of HA linkage, allowing for passive drug loading. Therefore, a combined passive and active drug loading approach was employed to co-load P18, P18 derivatives, and EPA within the liposome system. The liposomes demonstrated a LE exceeding 70 % for both EPA and P18, indicating the ideal capacity to accommodate both drugs (Fig. 1**C and D**). TEM images of Lip\EPA\P18 and Lip\EPA\P18-APBA demonstrated a nearly spherical shape, with a distinct fingerprint structure at the edge. While Lip\EPA\P18-APBA-HA appeared nearly spherical with a blurred fingerprint structure at the edge, attributed to the surface modification of HA (Fig. 1**E**). The UV–visible spectra of Lip\EPA\P18, Lip\EPA\P18-APBA, and Lip\EPA\P18-APBA-HA showed the characteristic peaks at 290 nm (EPA) and 406 nm (P18), confirming the effective loading of the two drugs into the formulation (Fig. 1**F**). The absorption peak of P18 at 695 nm showed a slight blue shift after the introduction of APBA, possibly due to the influence of interactions between APBA and P18, resulting in changes in the absorption peaks of Lip\EPA\P18-APBA and Lip\EPA\P18-APBA-HA [33].

In vitro photothermal performance of Lip|EPA|P18-APBA-HA

The photothermal performance of P18 was evaluated by monitoring its photothermal conversion at different concentrations and powers using an infrared thermal imaging camera (Fig. 1**G and H**). Initially, the impact of P18 concentration on photothermal conversion efficiency was examined under laser irradiation at 0.8 W/cm^2. The P18 solution temperature increased rapidly after 5 min of irradiation, with temperature amplitude intensifying proportionally to the concentration of P18. The temperature reached 42°C at a concentration of 2.5 μg/mL P18 and reached a maximum of 44°C at 5 μg/mL. According to previous research, high-temperature PTT (> 45°C) has been shown to induce irreversible damage to tumor cells, while mild PTT is more likely to trigger the ICD, thereby activating the systemic immune response [34,35]. We subsequently examined the effect of laser irradiation on the photothermal conversion efficiency was examined at a medium concentration of 2.5 μg/mL P18. Laser irradiation enhanced the photothermal performance of P18, with a more rapid temperature increase within 5 min when the power exceeded 0.8 W/cm^2. We then examined the photothermal performance of EPA + P18, Lip\EPA\P18, Lip\EPA\P18-APBA, and Lip\EPA\P18-APBA-HA at P18 2.5 μg/mL with 0.8 W/cm^2 laser irradiation. The infrared thermal images and corresponding temperature changes at different times were recorded (Fig. 1**I and J**). P18-APBA-HA, Lip\P18-APBA-HA, and Lip\EPA\P18-APBA-HA exhibited similar photothermal performance to P18, indicating that materials derived from P18 could maintain the potential of PTT by direct incorporation into liposomes. We assessed the photothermal stability of Lip\EPA\P18-APBA-HA (2.5 μg/mL P18) by exposure of the liposomal sample to a 671 nm laser at 0.8 W/cm^2, continuously turned on/off (5/5 min) for four cycles (Fig. 1**K**). The thermal fatigue loss was small over the four cycles, indicating that Lip\EPA\P18-APBA-HA had robust photothermal stability.

Effects of pH on diameter and zeta potential of Lip|EPA|P18-APBA-HA

At pH 7.4, the diameter and zeta potential of Lip\EPA\P18-APBA-HA remained relatively stable, while the diameter decreased by approximately 25 nm, the zeta potential increased by −12 mV at pH 6.5 (Fig. 1**L and Fig. S3**). This observation suggests that the alterations in the diameter and zeta potential of Lip\EPA\P18-APBA-HA may be attributed to the detachment of the outer modified HA caused by cleavage of the PBA ester bond at pH 6.5.

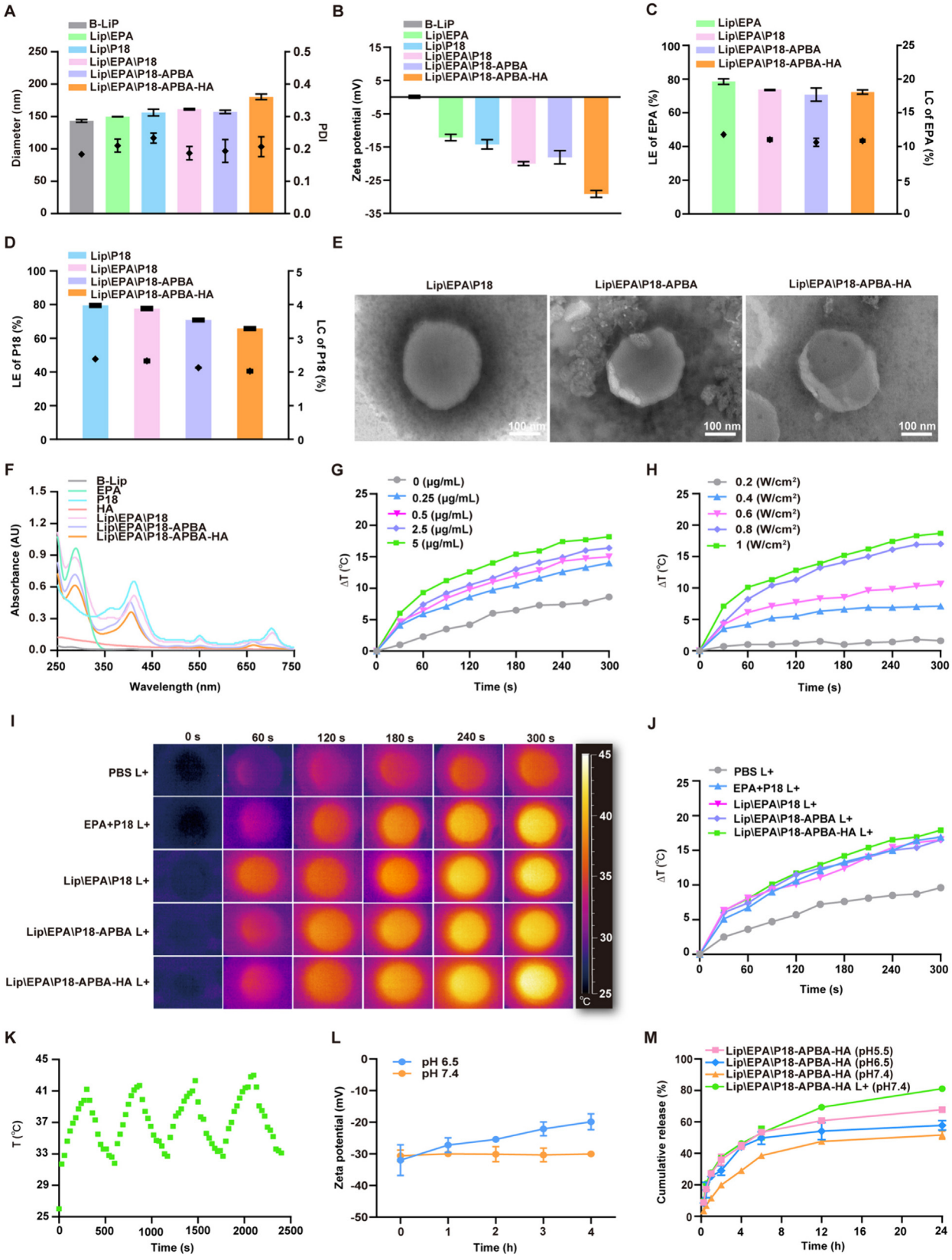

Fig. 1. Preparation and characterization of liposomes. (A) Liposome diameter (bars) and PDI (dots) and (B) zeta potential. (C, D) LE (bars) and LC (dots) of liposomes of EPA and P18. (E) Representative TEM images of Lip\EPA\P18, Lip\EPA\P18-APBA, and Lip\EPA\P18-APBA-HA (scale bar = 100 nm). (F) UV spectra of EPA, P18, HA, and liposomes. (G) Temperature changes of different concentrations of P18 (0–5 μg/mL) under 0.8 W/cm^2 laser irradiation. (H) Temperature changes of P18 under laser irradiation at different powers (0.2–1 W/cm^2). (I, J) Infrared thermal images and temperature changes under 0.8 W/cm^2 laser irradiation of PBS, EPA + P18, Lip\EPA\P18, Lip\EPA\P18-APBA, and Lip\EPA\P18-APBA-HA. (K) Temperature change curves of Lip\EPA\P18-APBA-HA solution under four cycles of irradiation. (L) Zeta potentials of Lip\EPA\P18-APBA-HA incubated at different pH values. (M) EPA release profiles of Lip\EPA\P18-APBA-HA at different pH values. L+ indicates liposomes exposed to 671 nm laser irradiation at 0.8 W/cm^2 for 5 min before dialysis. Data presented as mean ± SD (n = 3).

Drug release of Lip\EPA\P18-APBA-HA

The drug-release behavior of Lip\EPA\P18-APBA-HA was also investigated across varying pH conditions (Fig. 1**M**). The drug release of EPA from Lip\EPA\P18-APBA-HA was affected by pH, possibly attributed to reduced stability of the liposome system caused by the removal of HA under lower pH conditions. Removal of HA from the surface of the liposome also removed the hydrophilic shielding effect and the stabilizing effect conferred by the electronegativity of HA. Therefore, the stability of the system after HA removal is reduced compared with the existence of HA. In addition, we speculated that after P18-APBA-HA was stripped of HA to become P18-APBA under low pH conditions, might affect the insertion position of the material in the phospholipid bilayer, resulting in the perturbation of the phospholipid bilayer, and further decreasing the stability of the liposomes. Drug release from liposomes is a function of physical and chemical processes. When the stability of the liposome is reduced by physical or chemical factors can lead to partial or complete leakage of the liposome contents [36]. Therefore, we speculated that the HA removal from the surface slightly reduced the stability of the liposome and thus altered the kinetic behavior of the release of loaded EPA. Additionally, the release rate of EPA in Lip\EPA\P18-APBA-HA was significantly increased by laser irradiation. This observation may be attributed to the surface modification of liposomes by P18-APBA-HA mainly through the insertion of the hydrophobic part (P18) into the phospholipid bilayer. Consequently, laser exposure to P18-APBA-HA induces a temperature rise, thereby altering the fluidity of the phospholipid bilayer and facilitating the release of EPA. Taken together, this light-induced process may serve as a means of achieving targeted and controlled drug release from liposomes within the tumor site.

Cellular uptake

We prepared RB-loaded liposomes (**Fig. S4**) and evaluated the uptake capacity of B16F10 cells for the RB-loaded liposomes using a high-content imaging system. The fluorescence signal of free RB in tumor cells was weak at 2 and 4 h, while the fluorescence signal of RB-loaded liposomes was substantially intensified (Fig. 2**A and C**). This occurred because RB entered the cell via passive diffusion, while liposomes entered the cell through active transport, thereby maximizing the chance of cellular uptake by B16F10 cells through receptor-mediated endocytosis. Interestingly, Lip\RB\P18-APBA and Lip\RB\P18-APBA-HA showed significantly better uptake by tumor cells than Lip\RB\P18 under culture conditions of pH 6.5. To determine if the enhanced uptake of Lip\RB\P18-APBA-HA was mediated by the HA-CD44 ligand pathway, we pre-incubated HA to saturate the CD44 receptor on the surface of B16F10 cells. Blocking the CD44 receptor did not significantly decrease the uptake of Lip\RB\P18-APBA-HA, indicating that the uptake of Lip\RB\P18-APBA-HA by B16F10 cells may depend mainly on other routes. We subsequently pre-incubated APBA to saturate SA residues on the B16F10 cell surface, which significantly decreased the uptake of Lip\RB\P18-APBA-HA, indicating that Lip\RB\P18-APBA-HA primarily utilized APBA-SA-mediated cellular uptake as the primary pathway. The pH value of the TME typically ranges from 6.5 to 6.9, providing an optimal environment for tumor cell growth and metastasis [37]. The weakly acidic TME and the SA residues on the tumor cell surface will cause cleavage of the *iso*-PBA ester bond of P18-APBA-HA. We thus hypothesized that the surface HA of Lip\RB\P18-APBA-HA may detach at the tumor site, exposing more APBA on the liposome surface and restoring its specific targeting capability for SA residue's ability at the tumor site.

Intracellular ROS levels

B16F10 cells stained with DCFH-DA for ROS detection (Fig. 2**B and D**) were observed to have weak fluorescence in the PBS, EPA + P18, and Lip\EPA\P18-APBA-HA groups. However, laser irradiation enhanced the ROS signal in the tumor cells attributed to stimulation of P18 in its ground state, which then interacted with oxygen. Notably, significant ROS signals were detected in the cells in the Lip\EPA\P18-APBA and Lip\EPA\P18-APBA-HA groups. Combined with the results of the cell uptake experiment, Lip\EPA\P18-APBA and Lip\EPA\P18-APBA-HA groups could enhance P18 uptake by B16F10 cells via APBA-SA-mediated cell uptake as the main pathway. As a result, laser irradiation increased the ROS signals in these two groups.

Cytotoxicity assay

The toxicity of different concentrations of P18, EPA + P18, and Lip\EPA\P18-APBA-HA was investigated in the absence of light (Fig. 2**E**). Within a certain concentration range, P18, EPA + P18, and Lip\EPA\P18-APBA-HA showed no apparent inhibitory effect on tumor cells. This suggests that they had limited toxicity and high biocompatibility. However, upon laser exposure, the killing effect of EPA + P18 L+ on tumor cells increased significantly in a concentration-dependent manner (Fig. 2**F**). EPA did not contribute to the phototherapeutic effect, and cell killing was mainly achieved via the phototherapeutic effect of P18. Furthermore, Lip\EPA\P18-APBA L+ and Lip\EPA\P18-APBA-HA L+ induced cell death were increased compared with the free drug group, possibly due to enhanced cellular uptake. Previous tests showed that both free P18 and P18-loaded liposomes had photothermal response capabilities and could generate ROS in cells. Laser irradiation of the cells that internalized P18 and P18-loaded liposomes would thus produce a combined PDT/PTT effect. The high temperatures induced by PTT could directly cause cell death, while the ROS generated by PDT enhanced the thermosensitivity of the tumor cells.

Enhanced anti-tumor immunity in vitro

PIT can induce ICD, leading to the release of DAMPs as danger signals to activate DCs. These activated DCs then present tumor antigens to T cells, initiating tumor immune responses. We evaluated the induction of ICD by different formulations in B16F10 tumor cells by detecting three key DAMPs, CRT exposure, extracellular HMGB1, and ATP levels [38]. As shown in Fig. 3**A,** a neglectable green fluorescence signal was detected in all non-laser-treated groups. However, Lip\EPA\P18-APBA L+ and Lip\EPA\P18-APBA-HA L+ induced significant CRT exposure on cells, with stronger fluorescence intensity compared with the Lip\EPA\P18 L+ and EPA + P18 L+ groups. Meanwhile, laser irradiation increased extracellular HMGB1 and ATP secretion to varying degrees in each group (Fig. 3**B and C**). Notably, upregulation of CRT exposure, extracellular HMGB1, and ATP levels were significantly promoted in the Lip\EPA\P18-APBA L+ and Lip\EPA\P18-APBA-HA L+ groups, confirming their ability to induce the ICD in tumor cells through PIT. The suppression of IDO by EPA was determined by measuring the conversion of Kyn to Trp (Fig. 3**D**). Our results demonstrated that EPA, particularly in the Lip\EPA\P18-APBA L+ and Lip\EPA\P18-APBA-HA L+ groups reduced the Kyn/Trp ratio, possibly due to increased drug uptake through targeted modified nanocarriers. We also evaluated DC maturation by co-incubation of DC2.4 cells with B16F10 cells treated with various formulations. DC maturation was assessed by measuring the expression levels of the DC surface phenotypic marker molecules CD80 and CD86 (Fig. 3**E-G**). Even in the absence of light, both EPA + P18 and Lip\EPA\P18-APBA-HA affected DC maturation compared with the control group, possibly

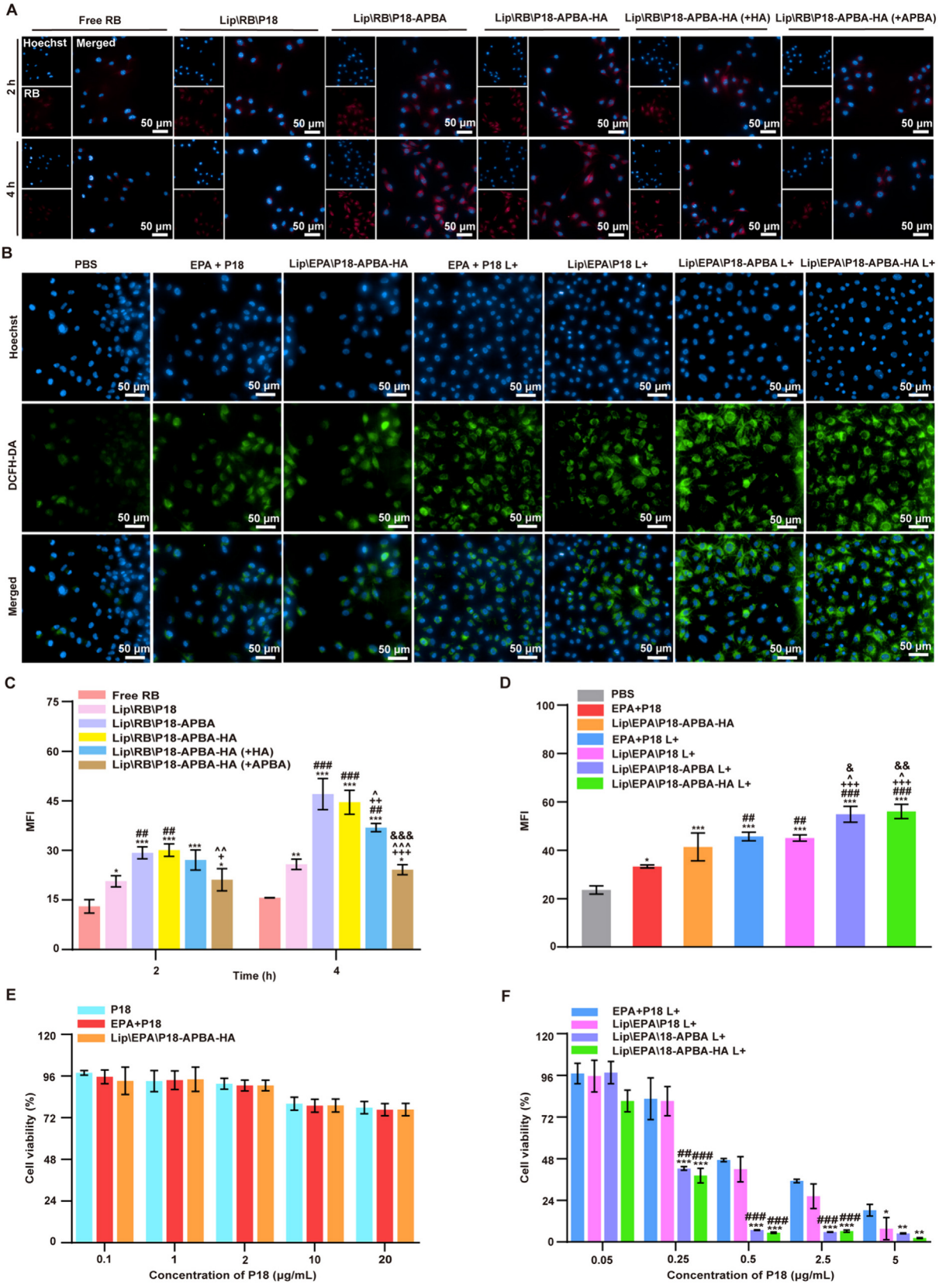

Fig. 2. *In vitro* cellular uptake, ROS generation, and cytotoxic effect. (A) B16F10 cells were incubated with free RB and RB-loaded liposomes for 2 and 4 h, respectively, and captured using a high-content imaging system (scale bar = 50 μm). (B) High-content images of ROS in B16F10 cells treated with different formulations with/without laser irradiation (scale bar = 50 μm). (C) Mean fluorescence intensity (MFI) of RB in B16F10 cells after incubation with free RB and RB-loaded liposomes for 2 and 4 h, respectively. $^{*}p < 0.05$, $^{**}p < 0.01$, $^{***}p < 0.001$ vs. free RB; $^{\#\#}p < 0.01$, $^{\#\#\#}p < 0.001$ vs. Lip\RB\P18; $^{+}p < 0.05$, $^{++}p < 0.01$, $^{++}p < 0.001$ vs. Lip\RB\P18-APBA; $^{\wedge}p < 0.05$, $^{\wedge\wedge}p < 0.01$, $^{\wedge\wedge\wedge}p < 0.001$ vs. Lip\RB\P18-APBA-HA; $^{\&\&\&}p < 0.001$ vs. Lip\RB\P18-APBA-HA (+HA). (D) MFI of intracellular DCF in cells treated with different formulations with/without laser irradiation. $^{*}p < 0.05$, $^{***}p < 0.001$ vs. PBS; $^{\#\#}p < 0.01$, $^{\#\#\#}p < 0.001$ vs. EPA + P18; $^{+++}p < 0.001$ vs. Lip\EPA\P18-APBA-HA; $^{\wedge}p < 0.05$ vs. EPA + P18 L+; $^{\&}p < 0.05$, $^{\&\&}p < 0.01$ vs. Lip\EPA\P18 L+. (E, F) Cytotoxic effects of P18, EPA + P18, Lip\EPA\P18, Lip\EPA\P18-APBA, and Lip\EPA\P18-APBA-HA with/without laser irradiation in B16F10 cells. $^{*}p < 0.05$, $^{**}p < 0.01$, $^{***}p < 0.001$ vs. EPA + P18 L+; $^{\#\#}p < 0.01$, $^{\#\#\#}p < 0.001$ vs. Lip\EPA\P18 L+. Data presented as mean ± SD (n = 3).

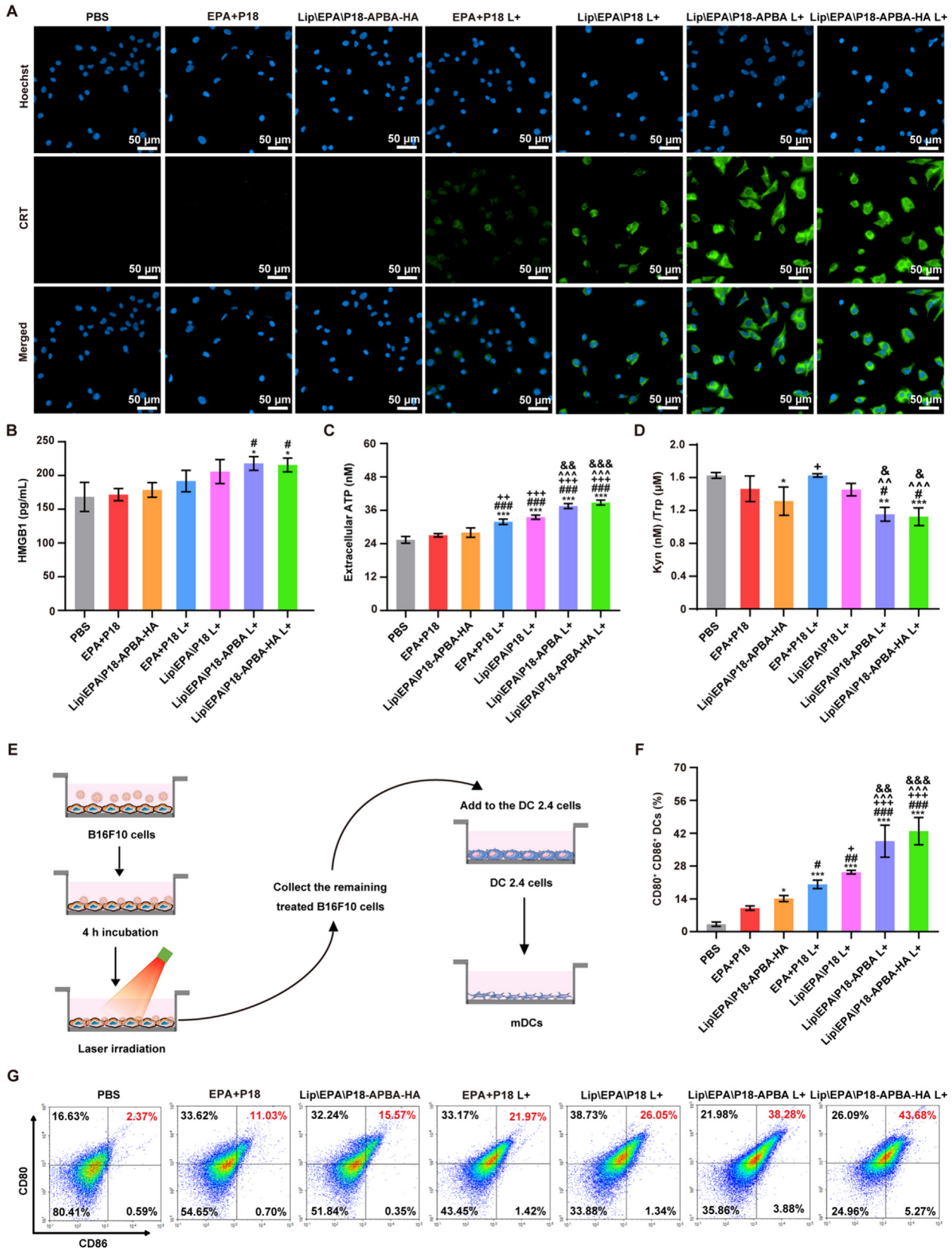

Fig. 3. *In vitro* enhancement of anti-tumor immunity under culture conditions. (A) High-content images showing the exposure of CRT on B16F10 cells after treatment with different formulations (scale bar = 50 μm). (B) Extracellular HMGB1 and (C) ATP levels following different treatments. (D) Quantification of Try/Kyn ratio in cell supernatants. (E) Schematic illustration of DC activation. B16F10 cells were treated with different formulations and co-cultured with DC2.4 cells, stained for various surface markers (CD80 and CD86), and then examined by FCM. (F, G) FCM quantification of CD80 and CD86 expression on DCs *in vitro*. $^{*}p < 0.05$, $^{**}p < 0.01$, $^{***}p < 0.001$ vs. PBS; $^{\#}p < 0.05$, $^{\#\#}p < 0.01$, $^{\#\#\#}p < 0.001$ vs. EPA + P18; $^{+}p < 0.05$, $^{++}p < 0.01$, $^{+++}p < 0.001$ vs. Lip\EPA\P18-APBA-HA; $^{\wedge\wedge}p < 0.01$, $^{\wedge\wedge\wedge}p < 0.001$ vs. EPA + P18 L+; $^{\&}p < 0.05$, $^{\&\&}p < 0.01$, $^{\&\&\&}p < 0.001$ vs. Lip\EPA\P18 L+. Data presented as mean ± SD (n = 3).

related to the drug-stimulating B16F10 cells promoting the release of TAAs. The CD80/CD86 ratio was higher in the Lip\EPA\P18-APBA L+ ($CD80^+$ $CD86^+$ 38.59%) and Lip\EPA\P18-APBA-HA L+ groups ($CD80^+$ $CD86^+$ 42.86%), suggesting the effective induction of DC maturation. Previous studies demonstrated that adequate levels of DC maturation were a prerequisite for T cell activation and subsequent cytotoxic effects on tumor cells. Additionally, IDO is highly expressed in tumor cells and antigen-presenting cells (APCs). IDO leads to the depletion of Trp and accumulation of Kyn in the TME, which inhibits the anti-tumor function of APCs and promotes the activation of Tregs to inhibit $CD8^+$ T cell activation [39,40].

Targeting effects of Cy5.5-loaded liposomes on tumors

Liposomes loaded with Cy5.5 were prepared (**Fig. S5**) for studying their biodistribution in B16F10 tumor-bearing mice *in vivo*. Free Cy5.5, Lip\Cy5.5\P18, Lip\Cy5.5\P18-APBA, and Lip\Cy5.5\P18-APBA-HA solutions were administered via the tail vein. The mice were anesthetized by isoflurane inhalation after 1, 2, 4, 6, 12, and 24 h, and images were obtained (Fig. 4**A**). Free Cy5.5 was distributed at the tumor region after 4 h, but the fluorescence signal decreased significantly after 12 h, indicating that Cy5.5 was rapidly metabolized and cleared by the body and did not easily accumulate in tumor tissue. Compared with the free Cy5.5 group, Cy5.5-loaded liposomes resulted in strong fluorescent signals in the primary tumors of tumor-bearing mice, and these signals gradually increased at the tumor sites within 12 h, indicating that Cy5.5-loaded liposomes could persist at the tumor site and were not easily cleared by the body. At 24 h after intravenous administration, the mice were sacrificed, and organs and tumors were separated. Photos were taken with a live-imaging system (Fig. 4**B**) and the distribution of Cy5.5 in each tissue was analyzed semi-quantitatively (Fig. 4**C**). Free Cy5.5 was primarily distributed in the liver and kidney, with almost no fluorescent signal at the tumor site. In contrast, fluorescence in the Cy5.5-loaded liposome group was distributed in the liver and kidney but also showed significant signals at the tumor region. Notably, the local fluorescent signal in tumors was stronger in the Lip\Cy5.5\P18-APBA-HA group than in the other groups. Lip\Cy5.5\P18-APBA-HA exhibited high targeting to tumor tissues, possibly due to its suitable particle size and long circulation protected by the HA hydrophilic shell. These features allow nanoparticles to leak through the blood circulation into the tumor neovascularization pores (200–600 nm in diameter) and utilize the EPR effect to accumulate in the tumor. Combined with the *in vitro* uptake results, once the HA-targeted nano-drug delivery system enters the tumor tissue extracellular space, it may also eliminate surface HA and expose APBA groups that can be specifically recognized by SA residues on the surface of melanoma cells, further enhancing the specific uptake of nanoparticles by melanoma cells [31]. However, compared with Lip\EPA\P18-APBA-HA, the distribution of Lip\EPA\P18-APBA in tumor sites was lower, and there was an off-target phenomenon. We evaluated the serum stability of each formulation by dispersing Lip\EPA\P18, Lip\EPA\P18-APBA, and Lip\EPA\P18-APBA-HA in PBS containing 10% (v/v) FBS at 37°C and monitored changes in diameter after incubation for 24 h. The diameter of Lip\EPA\P18-APBA-HA remained around 10 nm, indicating good serum stability. In contrast, the diameters of Lip\EPA\P18 and Lip\EPA\P18-APBA increased rapidly after incubation and then stabilized with no further diameter increase (**Fig. S6**). The Lip\EPA\P18-APBA-HA prepared in this study not only had a hydrophilic shielding effect generated by the surface HA but also had a strong surface potential (about −30 mV). The potential of Lip\EPA\P18 and Lip\EPA\P18-APBA liposomes was > −20 mV. Previous studies pointed out that liposomes with a zeta potential > +30 mV and <−30 mV) can maintain stable dispersion due to electrostatic mutual repulsion. However, the lower potential may tend to form unstable conditions such as aggregation, coagulation, and flocculation [41,42]. These results suggest that the hydrophilic modification of HA improved the stability of liposomes in serum, thereby prolonging liposome circulation time in the body. Lip\EPA\P18 and Lip\EPA\P18-APBA may have bound serum proteins during incubation, leading to a rapid increase in diameter, after which the particle size remained stable due to the stabilization of the adsorbed protein. After protein adsorption, the active targeting capacity would be reduced due to the shielding effect of the absorbed proteins [43,44].

Phototherapeutic effect of liposomes in primary tumors

We evaluated the phototherapeutic effect of each formulation in B16F10 tumor-bearing mice. PBS, EPA + P18, Lip\EPA\P18, Lip\EPA\P18-APBA, and Lip\EPA\P18-APBA-HA were administered intravenously. After 12 h, the tumor site was exposed to a 671 nm laser at 0.8 W/cm^2 for 2 min, and changes in tumor surface temperature were recorded (Fig. 4**D and E**). ROS generated in the tumors was detected by DCFH-DA after different treatments (Fig. 4**F and G**). There was no temperature increase in the PBS L+ group, excluding a local warming effect of laser irradiation itself on the mice. Temperatures in the EPA + P18 and Lip\EPA\P18 groups increased slightly after 2 min of irradiation but remained below 42°C. The Lip\EPA\P18-APBA and Lip\EPA\P18-APBA-HA groups exhibited higher tumor surface temperatures, exceeding 42°C. Regarding intra-tumoral ROS production, weak DCF fluorescence was detected in the PBS group, possibly due to an increase in the original ROS level of the tumor [45]. ROS levels also increased slightly in the EPA + P18 and Lip\EPA\P18-APBA-HA groups, likely due to drug stimulation. ROS signals in the tumors in the EPA + P18 L+, Lip\EPA\P18 L+, and Lip\EPA\P18-APBA L+ groups were significantly enhanced, possibly due to the PDT effect of a certain amount of P18 distributed in the tumor site after administration. The strongest ROS signal was detected in the Lip\EPA\P18-APBA-HA L+ group, which was in accordance with the tumor-targeting evaluation.

In vivo efficacy against primary tumors

B16F10 tumor-bearing mice were treated with different preparations containing EPA or P18. Tumor growth and general body condition were observed after 14 days, to evaluate the tumor inhibitory effect (Fig. 5**A**). The potential toxic and side effects of each preparation were evaluated by monitoring the changes in body weight of B16F10 model mice (Fig. 5**B**) and by routine blood tests. None of the mice showed any significant weight loss at 14 days, and there were no apparent differences in white blood cells, red blood cells, platelets, ALT, or AST in each preparation group compared with the PBS group (**Fig. S7**). Furthermore, histological analysis revealed no significant histological damage to any major organs after treatment with the various preparations (**Fig. S8**). These results indicated that the administered dosage was safe and there were no obvious toxic side effects in any of the preparation groups.

Changes and discrepancies in tumor volume within 14 days are shown in Fig. 5**C**. The mice were sacrificed on day 14 and the tumors were separated and photographed (Fig. 5**D**). The tumor volume in the PBS group increased rapidly, confirming the successful establishment of the model. The free EPA + P18 group exhibited weak tumor growth inhibition in the early stage (within 6 days), followed by a resumption of rapid growth in the later stage. The treatment effect of EPA + P18 L+ was slightly improved compared with the free EPA + P18 group. Importantly, the therapeutic effect of PIT treatment was significantly better compared with the other non-laser groups. Among these, the tumor growth rate was slower

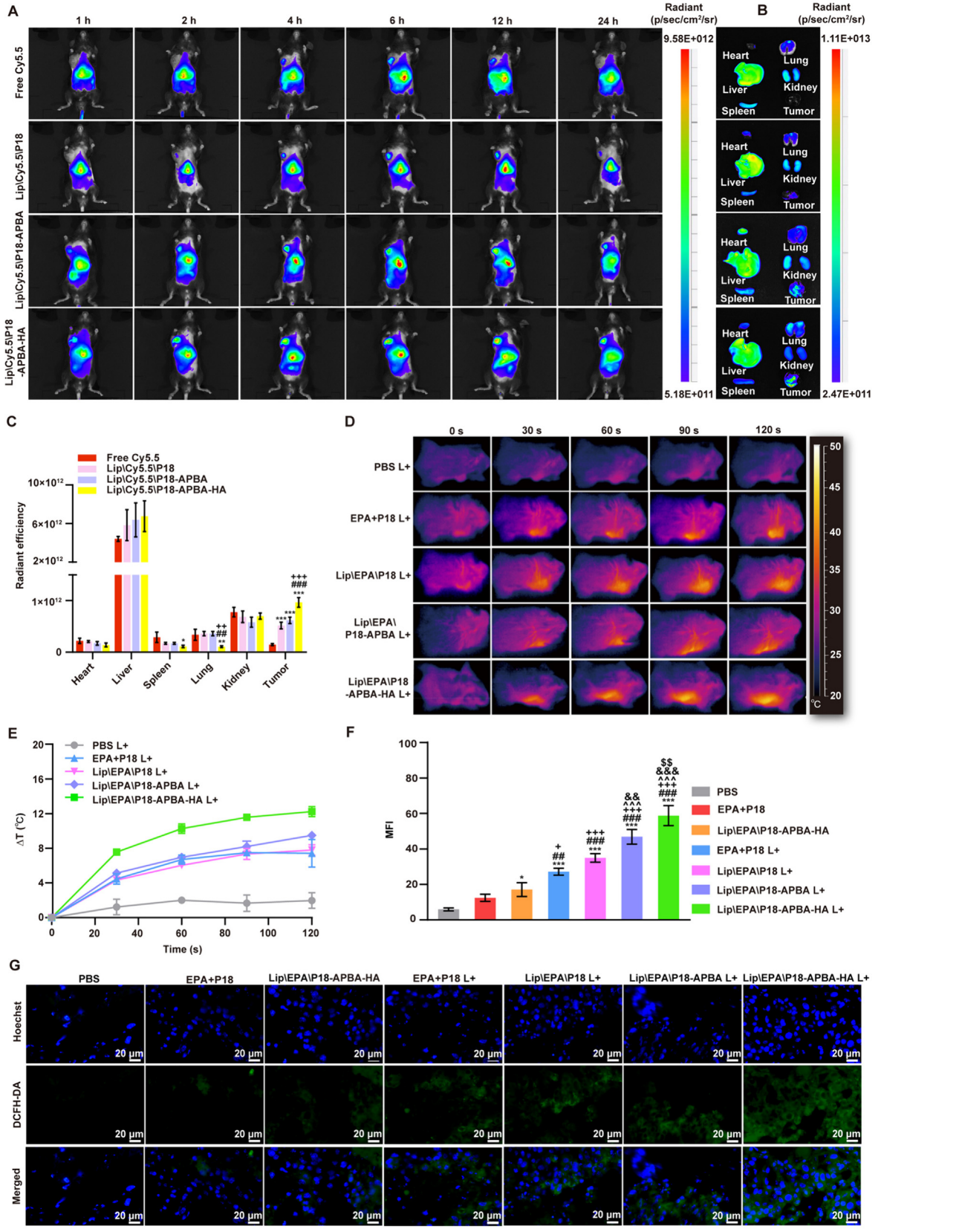

Fig. 4. *In vivo* biodistribution, PTT performance, and PDT efficiency of Lip\EPA\P18-APBA-HA. (A) Biodistribution of Cy5.5 in B16F10 tumor-bearing mice at 1, 2, 4, 6, 12, and 24 h post intravenous injection of free Cy5.5, Lip\Cy5.5\P18, Lip\Cy5.5\P18-APBA, and Lip\Cy5.5\P18-APBA-HA, respectively. (B, C) *Ex vivo* imaging and MFI quantification of transplanted heart, liver, spleen, lung, kidney, and tumor from mice at 24 h. $^{*}p < 0.05$, $^{**}p < 0.01$, $^{***}p < 0.001$ vs. free Cy5.5; $^{\#\#}p < 0.01$, $^{\#\#\#}p < 0.001$ vs. Lip\Cy5.5\P18; $^{++}p < 0.01$, $^{+++}p < 0.001$ vs. Lip\Cy5.5\P18-APBA. (D, E) Infrared thermal images and temperature change for mice following intravenous administration of different formulations followed by laser irradiation. (F, G) ROS detection in B16F10 tumor observed by CLSM (scale bar = 20 μm) and MFI quantification. $^{*}p < 0.05$, $^{***}p < 0.001$ vs. PBS; $^{\#\#}p < 0.01$, $^{\#\#\#}p < 0.001$ vs. EPA + P18; $^{+}p < 0.05$, $^{+++}p < 0.001$ vs. Lip\EPA\P18-APBA-HA; $^{\wedge\wedge\wedge}p < 0.001$ vs. EPA + P18 L+; $^{\&\&}p < 0.01$, $^{\&\&\&}p < 0.001$ vs. Lip\EPA\P18 L+; $^{\$\$}p < 0.01$ vs. Lip\EPA\P18-APBA L+. Data presented as mean ± SD (n = 3).

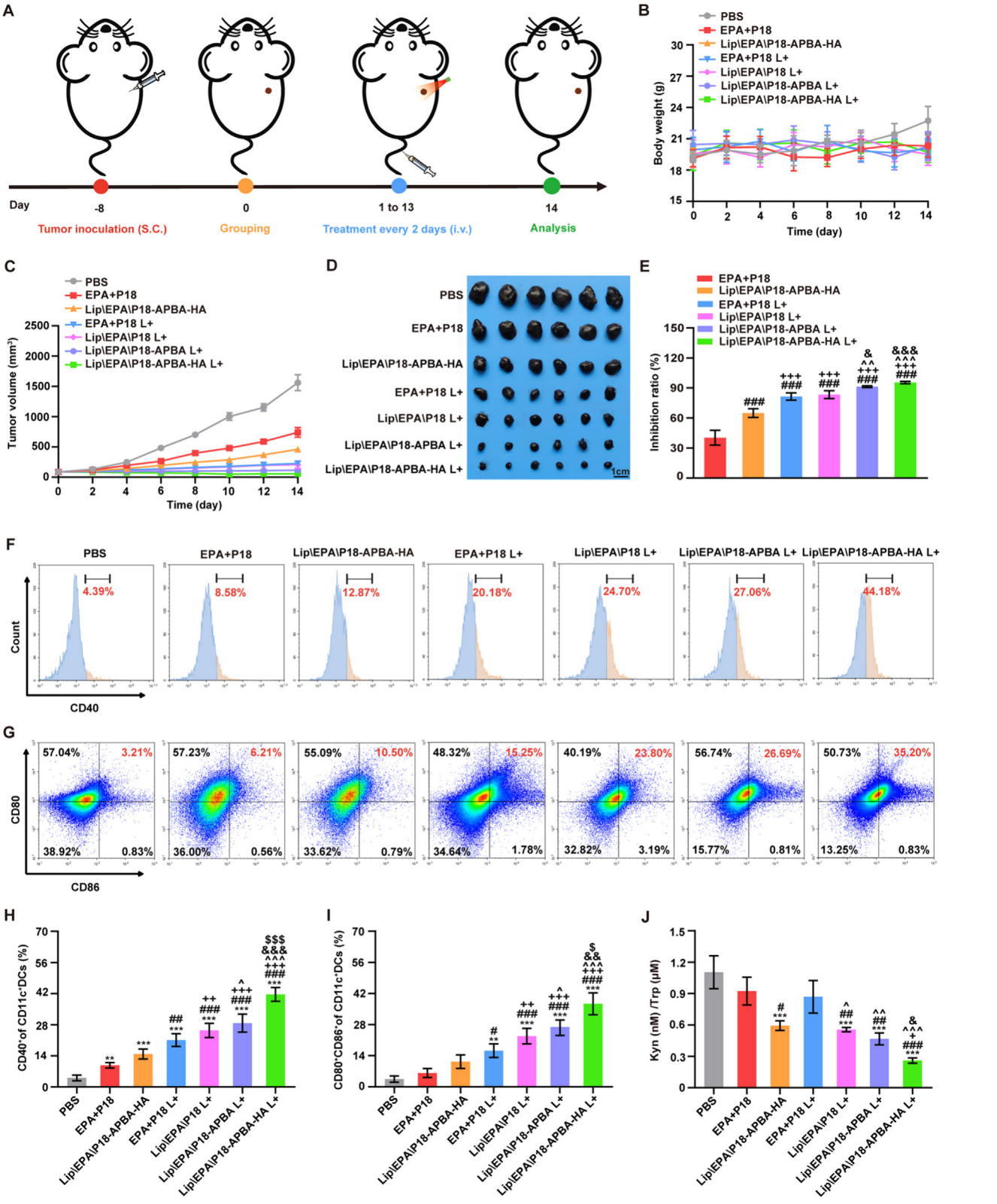

Fig. 5. *In vivo* therapeutic efficiencies of formulations against primary tumors and anti-tumor immunity. (A) Treatment schedule of anti-primary tumor experiments. (B) Change in body weight of B16F10 tumor-bearing mice (n = 6). (C) Primary tumor volume changes after various treatments (n = 6). (D) Images of excised tumors on day 14 (scale bar = 1 cm) (n = 6). (E) The inhibition ratio of tumor weight on day 14. (F-I) FCM analysis and percentage of mDCs ($CD40^+$, $CD80^+$ $CD86^+$) in TDLNs (n = 3). (J) Quantification of intratumoral Try/Kyn ratio in mice after different treatments (n = 3). $^{**}p < 0.01$, $^{***}p < 0.001$ vs. PBS; $^{\#}p < 0.05$, $^{\#\#}p < 0.01$, $^{\#\#\#}p < 0.001$ vs. EPA + P18; $^{+}p < 0.05$, $^{++}p < 0.01$, $^{+++}p < 0.001$ vs. Lip\EPA\P18-APBA-HA; $^{\wedge}p < 0.05$, $^{\wedge\wedge}p < 0.01$ $^{\wedge\wedge\wedge}p < 0.001$ vs. EPA + P18 L+; $^{\&}p < 0.05$, $^{\&\&}p < 0.01$, $^{\&\&\&}p < 0.001$ vs. Lip\EPA\P18 L+; $^{\$}p < 0.05$, $^{\$\$\$}p < 0.001$ vs. Lip\EPA\P18-APBA L+. Data presented as mean ± SD.

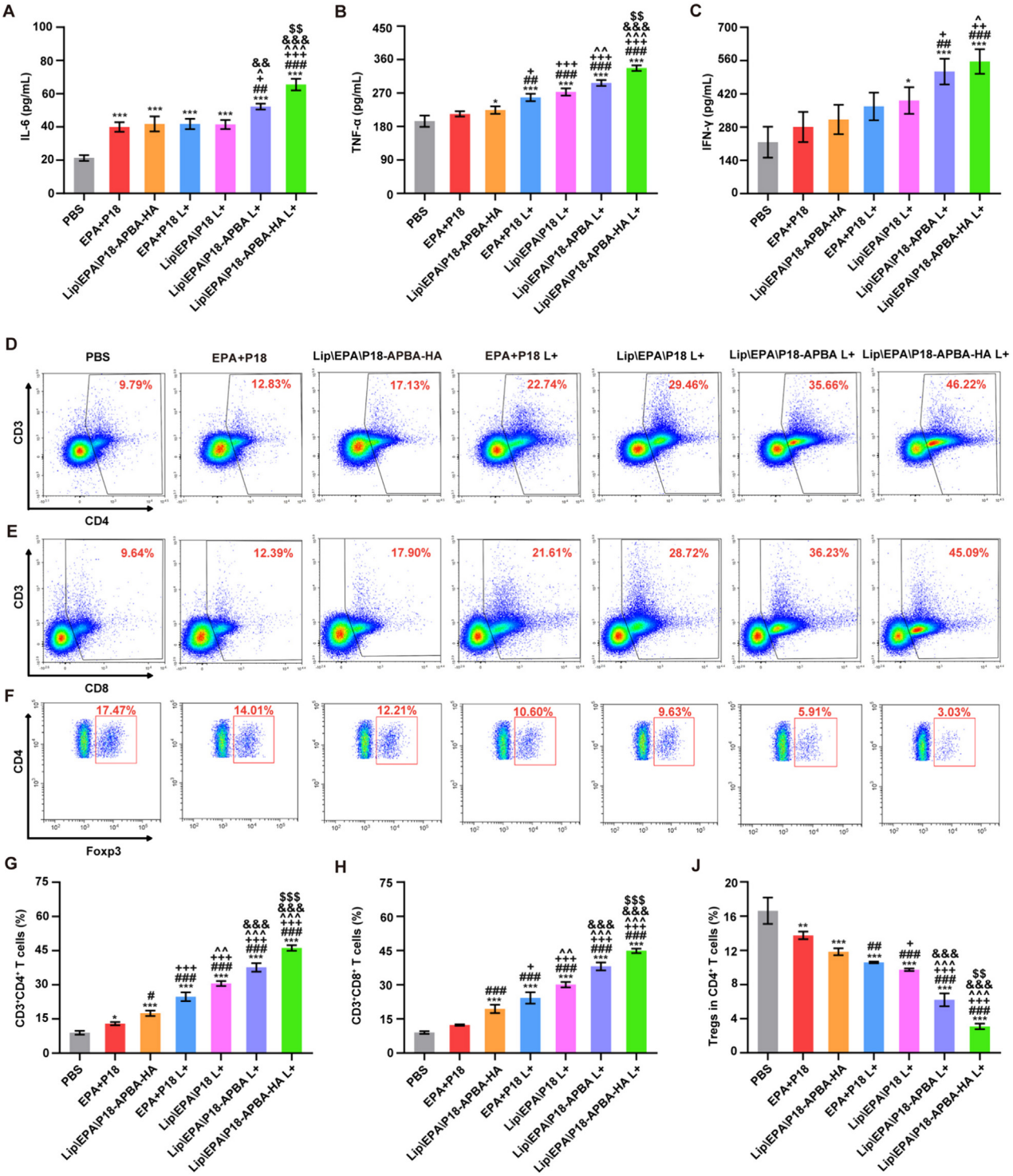

Fig. 6. *In vivo* anti-tumor immunity. Serum levels of (A) IL-6, (B) TNF-α, and (C) IFN-γ in mice after different treatments ($n = 3$). $^{*}p < 0.05$, $^{**}p < 0.01$, $^{***}p < 0.001$ vs. PBS; $^{\#}p < 0.05$, $^{\#\#}p < 0.01$, $^{\#\#\#}p < 0.001$ vs. EPA + P18; $^{+}p < 0.05$, $^{++}p < 0.01$, $^{+++}p < 0.001$ vs. Lip\EPA\P18-APBA-HA; $^{\wedge}p < 0.05$, $^{\wedge\wedge}p < 0.01$, $^{\wedge\wedge\wedge}p < 0.001$ vs. EPA + P18 L+; $^{\&\&\&}p < 0.01$, $^{\&\&\&}p < 0.001$ vs. Lip\EPA\P18 L+; $^{\$\$}p < 0.01$, $^{\$\$\$}p < 0.001$ vs. Lip\EPA\P18-APBA L+. Data presented as mean ± SD.

in the Lip\EPA\P18-APBA L + and Lip\EPA\P18-APBA-HA L+ groups over the 14 days. The tumor inhibition rates in terms of tumor weight in the Lip\EPA\P18-APBA L+ and Lip\EPA\P18-APBA-HA L+ groups on day 14 were 91.32% and 95.45%, respectively, showing no significant difference (Fig. 5**E**). These results indicated that Lip\EPA\P18-APBA L+ and Lip\EPA\P18-APBA-HA L+ exhibited enhanced tissue targeting capabilities, enabling easier delivery to the tumor site.

We further determined if the above formulations could trigger an immune response *in vivo*. The mice were sacrificed on day 14, DCs in TDLNs were collected and stained, and the maturated DCs (mDCs) were analyzed by FCM. DC maturation was quantified by

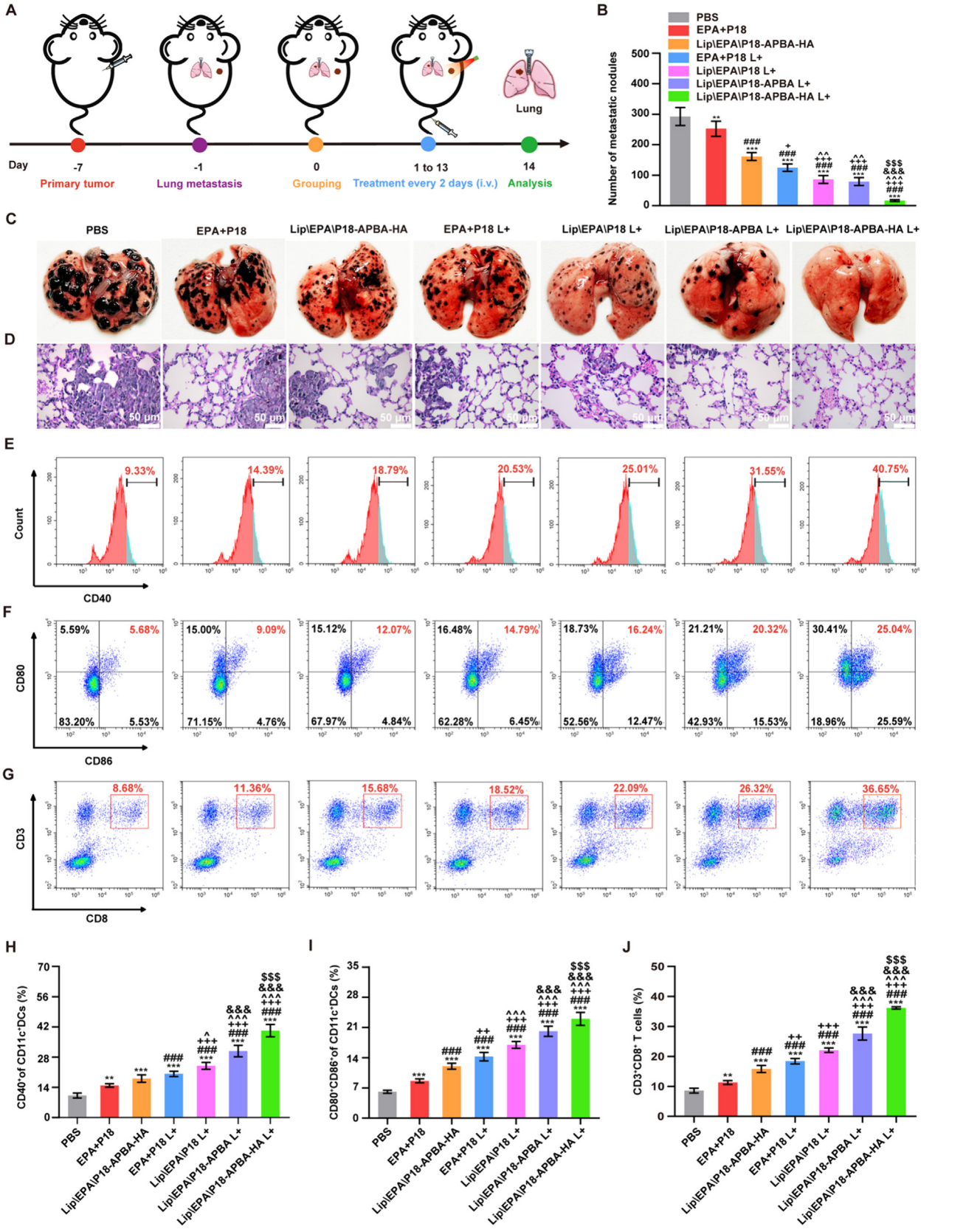

Fig. 7. In vivo anti-tumor lung metastasis efficacy. (A) Schematic illustration of anti-metastasis experiment. (B) Number of metastatic nodules in the lung (n = 6). (C, D) Images of metastatic nodules and H&E staining images in the lung (n = 6) (scale bar = 50 μm). FCM analysis and percentages of (E-I) mDCs ($CD40^+$, $CD80^+$ $CD86^+$) and (G, J) CTLs ($CD3^+$ $CD8^+$) in the lung (n = 6). $^{**}p < 0.01$, $^{***}p < 0.001$ vs. PBS; $^{\#\#\#}p < 0.001$ vs. EPA + P18; $^{+}p < 0.05$, $^{++}p < 0.01$, $^{+++}p < 0.001$ vs. Lip\EPA\P18-APBA-HA; $^{\wedge}p < 0.05$, $^{\wedge\wedge}p < 0.01$, $^{\wedge\wedge\wedge}p < 0.001$ vs. EPA + P18 L+; $^{\&\&\&}p < 0.001$ vs. Lip\EPA\P18 L+; $^{\$\$\$}p < 0.001$ vs. Lip\EPA\P18-APBA L+. Data presented as mean ± SD.

the expression of CD40, CD80, and CD86 markers (Fig. 5**F-I**). According to the previous studies [14], P18-mediated PDT and PTT could effectively stimulate DC maturation, and liposomes mediated P18 entry into tumor cells, which was in accordance with the *in vitro* research. The combination of EPA and P18, and Lip\EPA\P18-APBA-HA modestly stimulated tumor cells to release TAAs, leading to DC maturation. Interestingly, laser irradiation significantly enhanced DC maturation in all groups, particularly in the Lip\EPA\P18-APBA-HA L+ group ($CD40^+$ 41.63%, $CD80^+$ $CD86^+$ 37.35%). After reaching the tumor site, the surface modification of Lip\EPA\P18-APBA-HA facilitated the exposure of more target ligands through pH-response transformation, promoting internalization by tumor cells. *In vitro,* results indicated that increased uptake of drugs by tumor cells promoted the release of TAAs and subsequent activation of DC maturation. Therefore, Lip\EPA\P18-APBA-HA L+ effectively activated DC maturation. Furthermore, we examined the *in vivo* conversion of Trp to Kyn (Fig. 5**J**). Consistent with *in vitro* studies, free EPA + P18 and EPA + P18 L+ slightly down-regulated the Kyn/Trp ratio. Tumor targeting mediated by liposomes resulted in an increased drug concentration at the tumor site, leading to a significant decrease in the Kyn/Trp ratio in each drug-loaded liposome group. Interestingly, Lip\EPA\P18-APBA-HA L+ exhibited the most effective inhibition of IDO, possibly attributed to the enhanced-targeting design of the dual drug delivery system, which increased internalization of Lip\EPA\P18-APBA-HA into tumor cells and drug release with laser irradiation, thereby enhancing the inhibitory effect of EPA from Lip\EPA\P18-APBA-HA L+ on IDO in tumor cells. Immune-related cytokines also play a crucial role in anti-tumor immune responses. Th1-type cytokines, such as IL-6, TNF-α, and IFN-γ, primarily mediate cellular immunity and promote the cytotoxicity of CTLs [45,46]. Therefore, we collected serum samples from mice after the different treatments and analyzed these cytokines via ELISA (Fig. 6**A-C**). Drug-loaded liposomes exhibited higher immune intensity compared with the free drug group. Lip\EPA\P18-APBA-HA L+ resulted in the highest cytokine secretion, demonstrating the successful triggering of an immune response. Additionally, CTLs directly target and eliminate tumor cells and Th cells are crucial in the immune regulation process. Both CTLs and Th cells have key roles in the anti-tumor immune response, while Tregs regulate the immune response negatively and facilitate the escape from immune surveillance [46]. Therefore, we evaluated the infiltration of Th cells ($CD3^+$ $CD4^+$), CTLs ($CD3^+$ $CD8^+$), and Tregs ($CD4^+$ $Foxp3^+$) in tumors by FCM (Fig. 6**D-J**). Th cells and CTLs were increased, while Tregs decreased in all treatment groups, compared with the PBS group, with the highest levels of Th cells and CTLs and the lowest levels of Tregs in the Lip\EPA\P18-APBA-HA L+ treated group. The Th cells/Tregs and CTLs/Tregs ratios were 15.01 and 14.58, respectively (**Fig. S9**). These results indicate that Lip\EPA\P18-APBA-HA effectively eliminated primary tumors and stimulated strong anti-tumor immunity under laser irradiation.

In vivo anti-tumor lung metastasis efficacy

In this study, we established a mouse melanoma metastasis model and treated the mice with different treatments every 2 days. The mice were sacrificed on day 14 to assess the inhibitory effects of the drug combinations and carriers on lung metastasis (Fig. 7**A**). The metastatic nodules and morphology of the mouse lungs were studied to assess the efficacy of the preparations (Fig. 7**B and C**). The number of lung metastatic nodules was significantly decreased in the Lip\EPA\P18-APBA-HA L+ group compared with the Lip\EPA\P18 L+ and Lip\EPA\P18-APBA L+ groups, indicating the superior inhibitory effects of the Lip\EPA\P18-APBA-HA L+ preparation (Fig. 7**B**). We further assessed the therapeutic effect of each preparation by H&E staining of tissue sections (Fig. 7**D**). On day 14, the lung tissue structures in the PBS group were destroyed and the alveoli had disappeared. Tumor tissues in the EPA + P18 and Lip\EPA\P18-APBA-HA groups displayed infiltrative growth, and part of the lung tissue structure was destroyed. Smaller metastases were observed after exposure to light, with the most obvious anti-metastatic effect in the Lip\EPA\P18-APBA-HA L+ group. In conclusion, we found that this dual-drug delivery system provided the most effective treatment for melanoma metastasis, emphasizing the necessity of combining EPA and P18.

The anti-metastatic mechanism of the formulations in the lungs was further investigated using FCM. Mouse lungs were extracted on day 14 to assess DC maturation. Regardless of the markers used, the DC maturation rate in the free EPA + P18 group was approximately half that in the Lip\EPA\P18-APBA-HA L+ group. This confirmed that EPA + P18-loaded liposomes enhanced the maturation of DCs, particularly in combination with laser irradiation. In contrast to the *in vitro* results, Lip\EPA\P18-APBA-HA L+ was associated with greater DC maturation compared with Lip\EPA\P18-APBA L+ according to CD40 labeling (Fig. 7**E and H**) and CD80 and CD86 co-staining (Fig. 7**F and I**). Additionally, we evaluated the infiltration of CTLs ($CD3^+$ $CD8^+$) in the lungs (Fig. 7**G and J**). CTLs were significantly increased in each treatment group compared with the PBS group, especially in each liposome group. The proportions of CTLs in the Lip\EPA\P18-APBA L+ and Lip\EPA\P18-APBA-HA L+ groups were 3.22 times and 4.22 times than the PBS group, respectively. These results indicate that Lip\EPA\P18-APBA-HA L+ may enhance the immune response induced by TAAs, inhibit tumor cell metastasis, and achieve an optimal anti-melanoma therapeutic effect.

Conclusions

This study developed an HA-modified dual drug delivery system (Lip\EPA\P18-APBA-HA) to target melanoma. The HA coating enhanced the stability of the liposomes in serum and facilitated their accumulation at the tumor sites. At pH 6.5, Lip\EPA\P18-APBA-HA mainly utilized APBA-SA-mediated cellular uptake, demonstrating its efficacy in B16F10 cells, and indicating its potential for targeting tumor cells *in vivo*. Lip\EPA\P18-APBA-HA exhibited superior internalization by tumor cells in the TME via its two-stage targeted design. Furthermore, the intracellular release of EPA from Lip\EPA\P18-APBA-HA was triggered by thermal radiation, thereby inhibiting IDO activity in the TME, and promoting activation of the immune response. Consequently, Lip\EPA\P18-APBA-HA L+ effectively induced anti-tumor immunity by promoting DCs maturation, CTLs activation, Tregs suppression, and regulating cytokine secretion, to inhibit the proliferation of melanoma and lung metastasis. These findings suggest that the proposed targeted nano-drug delivery system provides a promising strategy for enhancing the inhibitory effects of the combination of EPA and P18 on melanoma proliferation and metastasis.

Compliance with Ethics Requirements

All animal procedures were performed in strict adherence to the protocol approved by the Animal Welfare and Ethics Committee of Guizhou Medical University (No. 1900118).

CRediT authorship contribution statement

Yi Chen: Investigation, Methodology, Writing – original draft, Writing – review & editing. **Shan Xu:** Investigation, Methodology, Data curation, Writing – original draft. **Shuang Ren:** Investigation,

Methodology, Data curation. **Jiyuan Zhang:** Investigation, Formal analysis. **Jinzhuan Xu:** Investigation, Formal analysis. **Yuxuan Song:** Investigation, Data curation. **Jianqing Peng:** Investigation, Data curation. **Shuai Zhang:** Conceptualization, Supervision, Writing – review & editing, Funding acquisition. **Qianming Du:** Conceptualization, Supervision, Writing – review & editing, Funding acquisition. **Yan Chen:** Conceptualization, Supervision, Writing – review & editing, Funding acquisition.

Declaration of competing interest

The authors declare that they have no known competing financial interests or personal relationships that could have appeared to influence the work reported in this paper.

Acknowledgements

This work was supported by the National Natural Science Foundation of China (81960333, 82373112, 82172558, 82273957), the Young Elite Scientists Sponsorship Program by CACM (CACM-(2023-QNRC2-B14), the Excellent Young Talents Plan of Guizhou Province (QKHPTRC(2021)-5632), the Guizhou Provincial Science and Technology Projects (QKHJC-ZK(2023)ZD-034), the Natural Science Foundation of Jiangsu (BK20231129), the Excellent Young Talents Plan of Guizhou Medical University (2020-101, 2021-103, 2023-102), the Guizhou Provincial Scientific and Technologic Innovation Base ([2023]003]), the State Key Laboratory of Guizhou Medical University (XZDSYS[2024]003), and the Guizhou Province High-level Innovative Talents Ten-Level Program (qiankehepingtairencai-GCC[2023]002).

Appendix A. Supplementary data

Supplementary data to this article can be found online at https://doi.org/10.1016/j.jare.2024.05.017.

References

[1] Deboever N, Feldman HA, Hofstetter WL, Mehran RJ, Rajaram R, Rice DC, et al. The role of surgery in the treatment of melanoma pulmonary metastases in the modern era. J Surg Res 2022;277:125–30. doi: https://doi.org/10.1016/j.jss.2022.04.021.

[2] Shain AH, Bastian BC. From melanocytes to melanomas. Nat Rev Cancer 2016;16:345–58. doi: https://doi.org/10.1038/nrc.2016.37.

[3] Phoon YP, Tannenbaum C, Diaz-Montero CM. Immunobiology of melanoma. Clin Plast Surg 2021;48:561–76. doi: https://doi.org/10.1016/j.cps.2021.06.005.

[4] Song M, Liu C, Chen S, Zhang W. Nanocarrier-based drug delivery for melanoma therapeutics. Int J Mol Sci 2021;22:1873. doi: https://doi.org/10.3390/ijms22041873.

[5] Zou J, Li L, Yang Z, Chen X. Phototherapy meets immunotherapy: a win–win strategy to fight against cancer. Nanophotonics 2021;10:3229. doi: https://doi.org/10.1515/nanoph-2021-0209.

[6] Wang M, Song J, Zhou F, Hoover AR, Murray C, Zhou B, et al. NIR-triggered phototherapy and immunotherapy via an antigen-capturing nanoplatform for metastatic cancer treatment. Adv Sci (Weinh) 2019;6:1802157. doi: https://doi.org/10.1002/advs.201802157.

[7] Jiang X, Yang M, Fang Y, Yang Z, Dai X, Gu P, et al. A photo-activated thermoelectric catalyst for ferroptosis-/pyroptosis-boosted tumor nanotherapy. Adv Healthc Mater 2023;12:e2300699.

[8] Kadkhoda J, Tarighatnia A, Barar J, Aghanejad A, Davaran S. Recent advances and trends in nanoparticles based photothermal and photodynamic therapy. Photodiagnosis Photodyn Ther 2022;37:102697. doi: https://doi.org/10.1016/j.pdpdt.2021.102697.

[9] Li W, Yang J, Luo L, Jiang M, Qin B, Yin H, et al. Targeting photodynamic and photothermal therapy to the endoplasmic reticulum enhances immunogenic cancer cell death. Nat Commun 2019;10:3349. doi: https://doi.org/10.1038/s41467-019-11269-8.

[10] Ng CW, Li J, Pu K. Recent progresses in phototherapy-synergized cancer immunotherapy. Adv Funct Mater 2018;28:1804688. doi: https://doi.org/10.1002/adfm.201804688.

[11] Yang W, Zhang F, Deng H, Lin L, Wang S, Kang F, et al. Smart nanovesicle-mediated immunogenic cell death through tumor microenvironment modulation for effective photodynamic immunotherapy. ACS Nano 2020;14:620–31. doi: https://doi.org/10.1021/acsnano.9b07212.

[12] Huang P, Zhang B, Yuan Q, Zhang X, Leung W, Xu C. Photodynamic treatment with purpurin 18 effectively inhibits triple negative breast cancer by inducing cell apoptosis. Lasers Med Sci 2021;36:339–47. doi: https://doi.org/10.1007/s10103-020-03035-w.

[13] Mishra PP, Datta A. Difference in the effects of surfactants and albumin on the extent of deaggregation of purpurin 18, a model of hydrophobic photosensitizer. Biophys Chem 2006;121:224–33. doi: https://doi.org/10.1016/j.bpc.2006.01.009.

[14] Sun Y, Zhang Y, Gao Y, Wang P, He G, Blum NT, et al. Six birds with one stone: versatile nanoporphyrin for single-laser-triggered synergistic phototheranostics and robust immune activation. Adv Mater 2020;32:e2004481.

[15] Xing L, Gong JH, Wang Y, Zhu Y, Huang ZJ, Zhao J, et al. Hypoxia alleviation-triggered enhanced photodynamic therapy in combination with IDO inhibitor for preferable cancer therapy. Biomaterials 2019;206:170–82. doi: https://doi.org/10.1016/j.biomaterials.2019.03.027.

[16] Sathyanarayanan V, Neelapu SS. Cancer immunotherapy: Strategies for personalization and combinatorial approaches. Mol Oncol 2015;9:2043–53. doi: https://doi.org/10.1016/j.molonc.2015.10.009.

[17] Peng J, Xiao Y, Li W, Yang Q, Tan L, Jia Y, et al. Photosensitizer micelles together with IDO inhibitor enhance cancer photothermal therapy and immunotherapy. Adv Sci (Weinh) 2018;5:1700891. doi: https://doi.org/10.1002/advs.201700891.

[18] Fujiwara Y, Kato S, Nesline MK, Conroy JM, DePietro P, Pabla S, et al. Indoleamine 2,3-dioxygenase (IDO) inhibitors and cancer immunotherapy. Cancer Treat Rev 2022;110:102461. doi: https://doi.org/10.1016/j.ctrv.2022.102461.

[19] Huang Z, Wei G, Zeng Z, Huang Y, Huang L, Shen Y, et al. Enhanced cancer therapy through synergetic photodynamic/immune checkpoint blockade mediated by a liposomal conjugate comprised of porphyrin and IDO inhibitor. Theranostics 2019;9:5542–57. doi: https://doi.org/10.7150/thno.35343.

[20] Jin SM, Lee SN, Kim JE, Yoo YJ, Song C, Shin HS, et al. Overcoming chemoimmunotherapy-induced immunosuppression by assemblable and depot forming immune modulating nanosuspension. Adv Sci (Weinh) 2021;8:e2102043.

[21] Shao J, Hou L, Liu J, Liu Y, Ning J, Zhao Q, et al. Indoleamine 2,3-dioxygenase 1 inhibitor-loaded nanosheets enhance CAR-T cell function in esophageal squamous cell carcinoma. Front Immunol 2021;12:661357. doi: https://doi.org/10.3389/fimmu.2021.661357.

[22] Tahaghoghi-Hajghorbani S, Yazdani M, Nikpoor AR, Hatamipour M, Ajami A, Jaafari MR, et al. Targeting the tumor microenvironment by liposomal Epacadostat in combination with liposomal gp100 vaccine. Sci Rep 2023;13:5802. doi: https://doi.org/10.1038/s41598-023-31007-x.

[23] Li L, Ni R, Zheng D, Chen L. Eradicating the tumor "seeds": nanomedicines-based therapies against cancer stem cells. Daru 2023;31:83. doi: https://doi.org/10.1007/s40199-023-00456-0.

[24] Makhani EY, Zhang A, Haun JB. Quantifying and controlling bond multivalency for advanced nanoparticle targeting to cells. Nano Converg 2021;8:38. doi: https://doi.org/10.1186/s40580-021-00288-1.

[25] Bai L, Yi W, Chen J, Wang B, Tian Y, Zhang P, et al. Two-stage targeted bismuthene-based composite nanosystem for multimodal imaging guided enhanced hyperthermia and inhibition of tumor recurrence. ACS Appl Mater Interfaces 2022;14:25050–64. doi: https://doi.org/10.1021/acsami.2c01128.

[26] Wang X, Cai H, Huang X, Lu Z, Zhang L, Hu J, et al. Chang, Formulation and evaluation of a two-stage targeted liposome coated with hyaluronic acid for improving lung cancer chemotherapy and overcoming multidrug resistance. J Biomater Sci Polym Ed 2023;34:1928–51. doi: https://doi.org/10.1080/09205063.2023.2201815.

[27] Kotla NG, Bonam SR, Rasala S, Wankar J, Bohara RA, Bayry J, et al. Recent advances and prospects of hyaluronan as a multifunctional therapeutic system. J Control Release 2021;336:598–620. doi: https://doi.org/10.1016/j.jconrel.2021.07.002.

[28] Li M, Sun J, Zhang W, Zhao Y, Zhang S, Zhang S. Drug delivery systems based on CD44-targeted glycosaminoglycans for cancer therapy. Carbohydr Polym 2021;251:117103. doi: https://doi.org/10.1016/j.carbpol.2020.117103.

[29] Khan T, Igarashi K, Tanabe A, Miyazawa T, Fukushima S, Miura Y, et al. Structural control of boronic acid ligands enhances intratumoral targeting of sialic acid to eradicate cancer stem-like cells. ACS Appl Bio Mater 2020;3:5030–9. doi: https://doi.org/10.1021/acsabm.0c00530.

[30] Lei L, Xu Z, Hu X, Lai Y, Xu J, Hou B, et al. Bioinspired multivalent peptide nanotubes for sialic acid targeting and imaging-guided treatment of metastatic melanoma. Small 2019;15:e1900157.

[31] Long Y, Lu Z, Mei L, Li M, Ren K, Wang X, et al. Enhanced melanoma-targeted therapy by "Fru-Blocked" phenyboronic acid-modified multiphase antimetastatic micellar nanoparticles. Adv Sci (Weinh) 2018;5:1800229. doi: https://doi.org/10.1002/advs.201800229.

[32] Tahaghoghi-Hajghorbani S, Khoshkhabar R, Rafiei A, Ajami A, Nikpoor AR, Jaafari MR, et al. Development of a novel formulation method to prepare liposomal Epacadostat. Eur J Pharm Sci 2021;165:105954. doi: https://doi.org/10.1016/j.ejps.2021.105954.

[33] Cheng DB, Qi GB, Wang JQ, Cong Y, Liu FH, Yu H, et al. In situ monitoring intracellular structural change of nanovehicles through photoacoustic signals based on phenylboronate-linked RGD-dextran/purpurin 18 conjugates.

Biomacromolecules 2017;18:1249–58. doi: https://doi.org/10.1021/acs.biomac.6b01922.
[34] Liu K, Zhang L, Lu H, Wen Y, Bi B, Wang G, et al. Enhanced mild-temperature photothermal therapy by pyroptosis-boosted ATP deprivation with biodegradable nanoformulation. J Nanobiotechnol 2023;21:64. doi: https://doi.org/10.1186/s12951-023-01818-1.
[35] Zhou Z, Jiang N, Chen J, Zheng C, Guo Y, Ye R, et al. Selectively down-regulated PD-L1 by albumin-phenformin nanoparticles mediated mitochondrial dysfunction to stimulate tumor-specific immunological response for enhanced mild-temperature photothermal efficacy. J Nanobiotechnol 2021;19:375. doi: https://doi.org/10.1186/s12951-021-01124-8.
[36] Maritim S, Boulas P, Lin Y. Comprehensive analysis of liposome formulation parameters and their influence on encapsulation, stability and drug release in glibenclamide liposomes. Int J Pharm 2021;592:120051. doi: https://doi.org/10.1016/j.ijpharm.2020.120051.
[37] Kooshki L, Mahdavi P, Fakhri S, Akkol EK, Khan H. Targeting lactate metabolism and glycolytic pathways in the tumor microenvironment by natural products: a promising strategy in combating cancer. Biofactors 2022;48:359–83. doi: https://doi.org/10.1002/biof.1799.
[38] Zhang Y, Guo C, Liu L, Xu J, Jiang H, Li D, et al. ZnO-based multifunctional nanocomposites to inhibit progression and metastasis of melanoma by eliciting antitumor immunity via immunogenic cell death. Theranostics 2020;10:11197–214. doi: https://doi.org/10.7150/thno.44920.
[39] Chen Y, Du Q, Zou Y, Guo Q, Huang J, Tao L, et al. Co-delivery of doxorubicin and epacadostat via heparin coated pH-sensitive liposomes to suppress the lung metastasis of melanoma. Int J Pharm 2020;584:119446. doi: https://doi.org/10.1016/j.ijpharm.2020.119446.
[40] Nijen Twilhaar MK, Czentner L, Bouma RG, Olesek K, Grabowska J, Wang AZ, et al. Incorporation of toll-like receptor ligands and inflammasome stimuli in GM3 liposomes to induce dendritic cell maturation and T cell responses. Front Immunol 2022;13:842241. doi: https://doi.org/10.3389/fimmu.2022.842241.
[41] Manaia EB, Abuçafy MP, Chiari-Andréo BG, Silva BL, Oshiro Junior JA, Chiavacci LA. Physicochemical characterization of drug nanocarriers. Int J Nanomedicine 2017;12:4991–5011. doi: https://doi.org/10.2147/IJN.S133832.
[42] Németh Z, Csóka I, Semnani Jazan R, Sipos B, Haspel H, Kozma G, et al. Quality by design-driven zeta potential optimisation study of liposomes with charge imparting membrane additives. Pharmaceutics 2022;14:1798. doi: https://doi.org/10.3390/pharmaceutics14091798.
[43] Xiao Q, Zoulikha M, Qiu M, Teng C, Lin C, Li X, et al. The effects of protein corona on in vivo fate of nanocarriers. Adv Drug Deliv Rev 2022;186:114356. doi: https://doi.org/10.1016/j.addr.2022.114356.
[44] Xu M, Qi Y, Liu G, Song Y, Jiang X, Du B. Size-dependent in vivo transport of nanoparticles: implications for delivery, targeting, and clearance. ACS Nano 2023;17:20825–49. doi: https://doi.org/10.1021/acsnano.3c05853.
[45] Zhang Y, Du X, Liu S, Yan H, Ji J, Xi Y, et al. NIR-triggerable ROS-responsive cluster-bomb-like nanoplatform for enhanced tumor penetration, phototherapy efficiency and antitumor immunity. Biomaterials 2021;278:121135. doi: https://doi.org/10.1016/j.biomaterials.2021.121135.
[46] Zhang D, Zhang J, Li Q, Song A, Li Z, Luan Y. Cold to hot: Rational design of a minimalist multifunctional photo-immunotherapy nanoplatform toward boosting immunotherapy capability. ACS Appl Mater Interfaces 2019;11:32633–46. doi: https://doi.org/10.1021/acsami.9b09568.